RSC Advances

PAPER

View Article Online
View Journal | View Issue

Cite this: *RSC Adv.*, 2026, **16**, 30052

Design, synthesis, and mechanistic evaluation of novel pyrazole/thiazole chalcone hybrids as dual tubulin polymerization and COX-2 inhibitors with potent antiproliferative activity

Basima A. A. Saleem, [a] Ashraf A. Qurtam, [b] Abdelrahman R. Shalabi, [c] Mohammed Al-zharani, [b] Kasim Sakran Abass, *[d] Stefan Bräse, [e] Ghallab Alotaibi [f] and Abdullah Alkhammash [f]

A novel series of pyrazole/thiazole chalcone hybrids (**9a–o**) was designed, synthesized, and evaluated as dual tubulin/COX-2 inhibitors with anticancer activity. The synthesized compounds were screened for antiproliferative activity against MDA-MB-231, HCA-7, and A549 cancer cell lines. Several derivatives exhibited promising activity, with **9m** being the most potent against MDA-MB-231 cells (IC_{50} = 1.96 ± 0.10 μM), while **9l** emerged as the most balanced lead compound, showing strong antiproliferative activity against HCA-7, MDA-MB-231, and A549 cells with IC_{50} values of 2.18 ± 0.11, 2.92 ± 0.15, and 4.86 ± 0.25 μM, respectively. Mechanistic studies revealed that the anticancer activity of this series is mediated through a dual mechanism involving tubulin polymerization inhibition and selective COX-2 inhibition. In particular, compound **9l** inhibited tubulin polymerization with an IC_{50} of 4.21 ± 0.25 μM and showed potent COX-2 inhibition (IC_{50} = 0.10 ± 0.01 μM) with high selectivity over COX-1 (IC_{50} = 10.92 ± 0.78 μM; selectivity index = 109.20). Further investigation in HCA-7 cells demonstrated that **9l** significantly increased Bax level to 438.64 ± 15.72 pg mL^{-1} and reduced Bcl-2 to 6.74 ± 0.19 pg mL^{-1}, while markedly elevating caspase-3 and caspase-9 levels to 496.80 ± 14.90 pg mL^{-1} and 47.86 ± 1.18 ng mL^{-1}, respectively. Moreover, **9l** strongly suppressed PGE-2 production to 0.56 ± 0.04 ng mL^{-1}, corresponding to 89.2% inhibition, and induced G2/M cell-cycle arrest. It also showed promising anti-migratory activity in the wound-healing assay, favorable microsomal stability, and acceptable *in silico* ADMET properties. Molecular docking further supported its favorable binding within the active sites of both tubulin and COX-2. Collectively, these findings identify **9l** as a promising dual tubulin/COX-2-targeting anticancer candidate.

Received 26th April 2026
Accepted 22nd May 2026

DOI: 10.1039/d6ra03557d

rsc.li/rsc-advances

1. Introduction

Cancer remains one of the leading causes of death worldwide and continues to impose a major therapeutic burden despite substantial advances in surgery, radiotherapy, and systemic treatment.[1] Its lethality is driven not only by uncontrolled proliferation but also by invasion, metastasis, and the progressive acquisition of resistance to therapy.[2,3] According to the World Health Organization, cancer accounted for nearly 10 million deaths in 2020,[4] and roughly one-third of cancer deaths are linked to modifiable risk factors such as tobacco use, alcohol consumption, obesity, unhealthy diet, and physical inactivity. These realities continue to justify the search for mechanistically innovative small molecules capable of interfering with multiple cancer-relevant pathways simultaneously.[5–8]

Among validated anticancer strategies, disruption of microtubule dynamics remains one of the most successful approaches in medicinal chemistry.[9] Microtubules are dynamic polymers of α/β-tubulin heterodimers that are essential for cell architecture, intracellular transport, and, most importantly, chromosome segregation during mitosis.[10] Agents that inhibit tubulin polymerization suppress spindle formation, arrest cells at the G2/M phase, and ultimately promote apoptotic death.[11]

[a]*Department of Chemistry, College of Science, University of Mosul, Mosul 41001, Iraq*
[b]*Biology Department, College of Science, Imam Mohammad Ibn Saud Islamic University (IMSIU), Riyadh 11623, Saudi Arabia*
[c]*Pharmaceutical Chemistry Department, Faculty of Pharmacy, Sinai University, North Sinai, Egypt*
[d]*Department of Physiology, Biochemistry and Pharmacology, College of Veterinary Medicine, University of Kirkuk, Kirkuk 36001, Iraq. E-mail: kasim_abass@uokirkuk.edu.iq*
[e]*Institute of Biological and Chemical Systems—Functional Molecular Systems (IBCS-FMS), Karlsruhe Institute of Technology (KIT), Kaiserstrasse 12, 76131 Karlsruhe, Germany*
[f]*Department of Pharmacology, College of Pharmacy, Al-Dawadmi Campus, Shaqra University, Shaqra 11961, Saudi Arabia*

Within this class, ligands that target the colchicine-binding site are especially attractive because they prevent tubulin from adopting the conformation required for microtubule assembly, and combretastatin A-4 (CA-4) remains one of the best-known prototypes.[12] However, the therapeutic exploitation of CA-4 has been limited by drawbacks associated with its *cis*-stilbene system, especially its tendency to lose the active geometry and related pharmaceutical limitations,[13] which has encouraged the development of structurally constrained mimics and heterocyclic replacements.

In this context, both thiazoles and chalcones have emerged as highly valuable motifs in the design of tubulin polymerization inhibitors.[14] Thiazole-containing scaffolds are well-established in anticancer drug discovery, where they serve as rigid heteroaromatic frameworks suitable for colchicine-site binding.[15–17] Likewise, chalcones offer a privileged aryl–enone scaffold capable of occupying hydrophobic regions within the tubulin pocket and promoting antiproliferative activities.[18,19] The [2,1-*b*]thiazole–chalcone conjugate I illustrates this, exhibiting broad cytotoxicity alongside microtubule disruption, G2/M arrest, and induction of apoptosis.[20] The benzo[*d*]imidazo[2,1-*b*]thiazole–chalcone hybrid **II** similarly demonstrated effective inhibition of tubulin assembly with consequent mitotic arrest.[21] In addition, the thiazole-based chalcone **III** highlighted the intrinsic potential of this hybrid framework as a tubulin-targeting pharmacophore.[22] This strategy was further substantiated by compounds **IV** and **V**, which combined tubulin interference with carbonic anhydrase IX inhibition.[23,24] In another study, the bisthiazole chalcone **VI** exhibited pronounced anti-tubulin activity, with clear cell-cycle arrest and apoptotic effects in MCF-7 cells.[25] Similarly, the thiazole-2-acetamide derivative **VII** displayed potent tubulin-associated antiproliferative activity accompanied by apoptosis induction.[26] The structures of these representative compounds are shown in Fig. 1. Collectively, these findings reinforce the versatility of thiazole–chalcone hybrids as antimitotic agents.

A second pathway highly relevant to malignant progression is the cyclooxygenase pathway, particularly COX-2.[27] COX-1 is constitutively expressed and is involved in homeostatic functions such as gastric mucosal protection and platelet physiology, whereas COX-2 is an inducible isoform that becomes markedly upregulated during inflammation and in many tumors.[28] Beyond its role in inflammation, COX-2 contributes to several hallmarks of cancer by promoting prostaglandin-dependent proliferation, angiogenesis, migration, invasion, immune evasion, and resistance to apoptosis.[29] These findings explain the continued interest in selective COX-2 inhibitors as anticancer agents.[29,30] Classical coxibs such as celecoxib, rofecoxib, valdecoxib, and etoricoxib were developed to exploit structural differences between COX-1 and COX-2, particularly the larger secondary side pocket in COX-2. However, safety concerns have limited the use of some members of this class.[31,32] Even so, the COX-2/PGE_2 axis remains an attractive target for hybrid anticancer design.

The pyrazole ring is regarded as a privileged scaffold in medicinal chemistry because of its broad and well-documented spectrum of pharmacological activities, including analgesic, anti-inflammatory, anticancer, antimicrobial, and CNS effects.[33,34] In particular, pyrazole-based compounds are well-established in NSAID chemistry and have been widely exploited in the design of COX-2-directed agents.[35] Several marketed NSAID-related drugs also contain a pyrazole core, such as celecoxib, tepoxalin, lonazolac, and difenamizole.[36] This importance is further underscored by several reports on pyrazole-based selective COX-2 inhibitors (Fig. 2). For example, pyrazole-1,3,4-oxadiazole hybrid **VIII** exhibited selective COX-2 inhibition, along with anti-inflammatory, analgesic, and gastro-sparing properties.[37] Similarly, pyrazole–chrysin hybrid **IX** combined selective COX-2 inhibition with antiproliferative activity.[38] Likewise, pyrazole–thiadiazole hybrid **X** emerged as a highly selective COX-2 inhibitor with a favorable drug-likeness profile,[39] whereas more recent difenamizole-inspired pyrazole **XI** bearing a bulkier *N*-substituent showed improved COX-2 selectivity together with EGFR inhibition.[40]

1.1 Rational design

The simultaneous targeting of tubulin polymerization and COX-2 is biologically and pharmacologically justified. Tubulin inhibition disrupts mitotic spindle formation and promotes

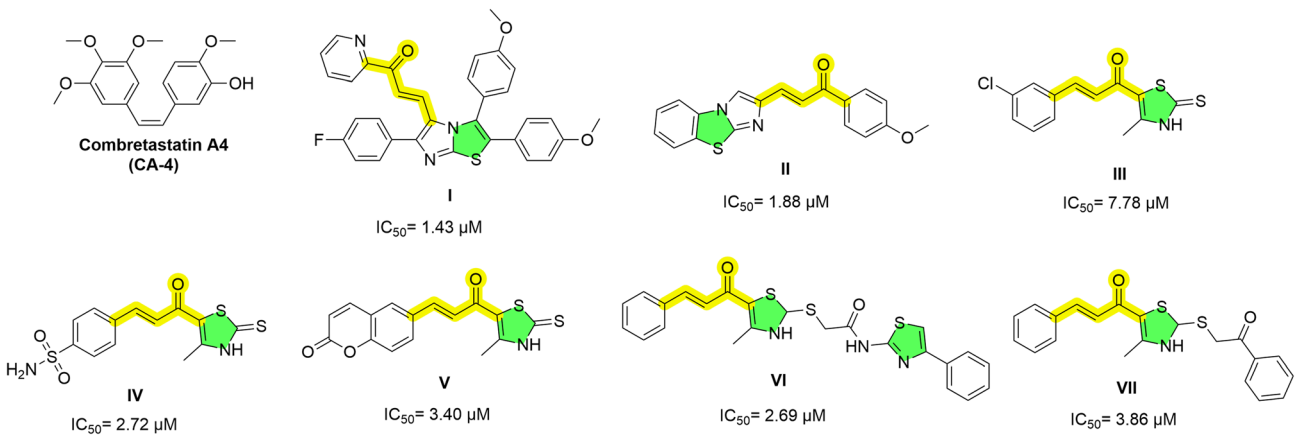

Fig. 1 Selected thiazole/chalcone-based tubulin polymerization inhibitors (I–VII) and combretastatin A-4.

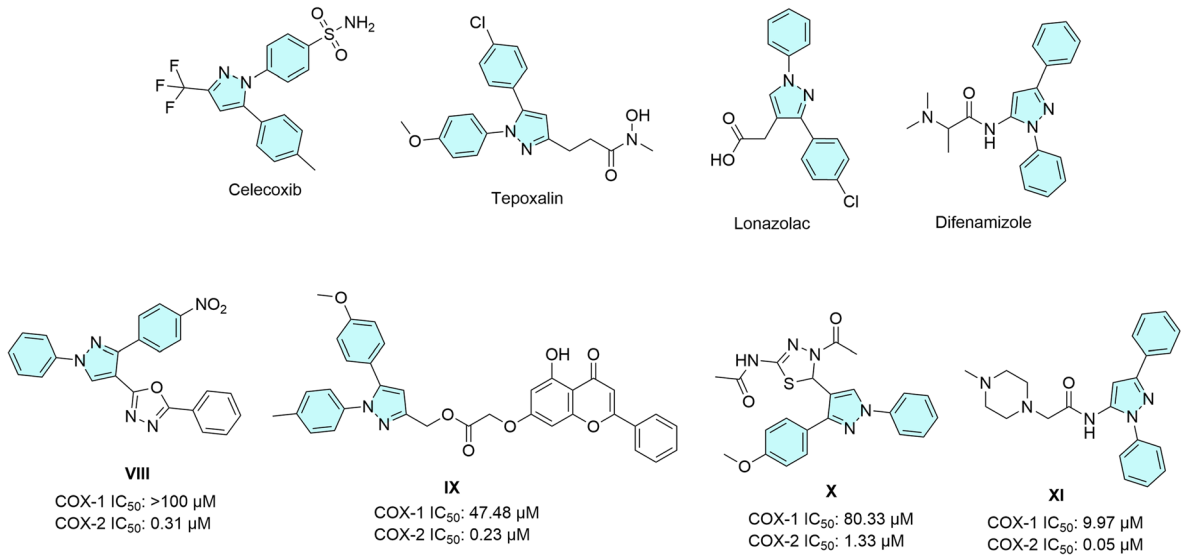

Fig. 2 Selected pyrazole-containing drugs and pyrazole-based selective COX-2 inhibitors (**VIII–XI**).

apoptotic cell death, whereas COX-2 inhibition is expected to suppress prostaglandin-driven signaling involved in tumor growth, angiogenesis, invasion, and resistance to apoptosis. This concept is supported by both preclinical and clinical evidence, including studies of celecoxib combined with taxane-based regimens.[41–43] Moreover, the feasibility of integrating both activities within a single scaffold has already been demonstrated through molecular hybridization; notably, the rofecoxib/combretastatin hybrid KSS19 was designed to unite COX-2 inhibition with microtubule-disrupting activity while avoiding the *cis–trans* isomerization liability of CA-4, and later coxib–combretastatin hybrids likewise confirmed the potential of combining antiproliferative and anti-inflammatory properties within one molecule.

Guided by these considerations, the present design was developed to integrate tubulin polymerization inhibition and COX-2 targeting within a single hybrid molecule (Fig. 3). From the tubulin perspective, it was guided by the classical ring A-

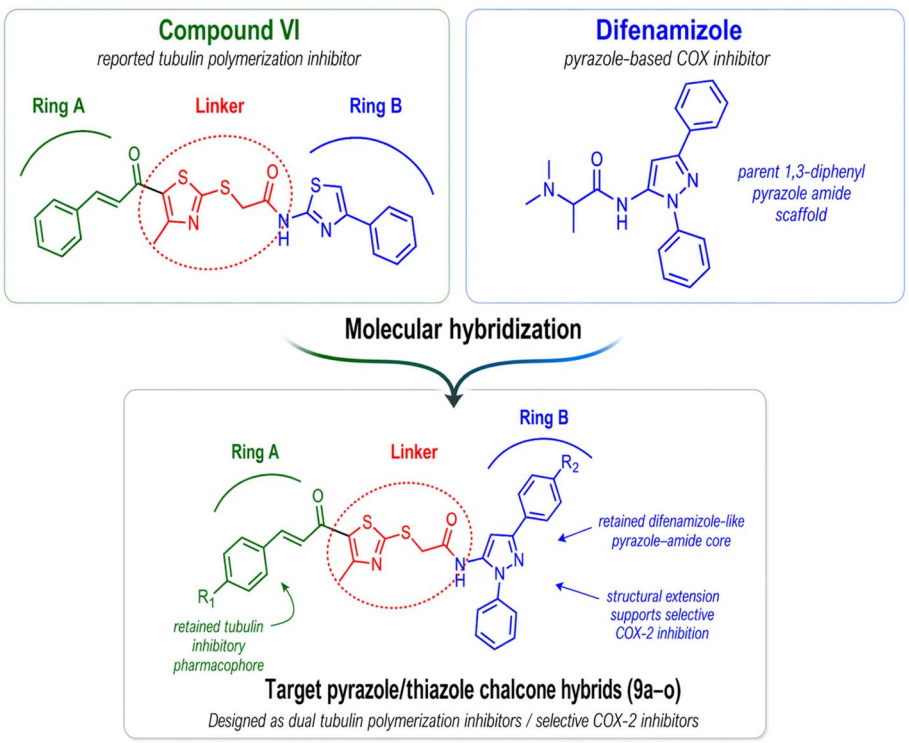

Fig. 3 Rational design of the target hybrids **9a–o**.

linker-ring B organization of CA-4-inspired colchicine-site inhibitors. In the current series, ring A consisted of a thiazole–chalcone fragment, selected as an extended hydrophobic pharmacophore capable of occupying the lipophilic region of the colchicine-binding pocket while also acting as a conformationally restricted replacement for the labile *cis*-stilbene system of CA-4. The linker incorporated a thioacetamide spacer, whereas ring B was introduced as a 1,3-diphenylpyrazole unit, chosen as a heteroaromatic moiety expected to establish favorable hydrophobic interactions within adjacent regions of the colchicine-binding site while also providing a COX-2-relevant structural element within the same framework.

More specifically, ring B was selected as a 1,3-diphenylpyrazole unit because the pyrazole nucleus represents the key heterocyclic motif of difenamizole, whereas the diphenyl substitution was expected to provide the steric expansion required for preferential accommodation within the larger COX-2 secondary pocket relative to COX-1. Applying this principle, the current design retained the 1,3-diphenylpyrazole–amide core while replacing the smaller dimethylamino substituent in difenamizole with a more extended thiazole–chalcone moiety. This modification was expected not only to favor binding to COX-2 but also to introduce a tubulin-directed pharmacophore. In addition, variation at the chalcone aryl ring and the 3-phenyl substituent of the pyrazole nucleus was intended to fine-tune hydrophobic and physicochemical features across both targets, thereby supporting the development of dual-acting anticancer candidates.

2. Results and discussion

2.1 Chemistry

The target compounds **9a–o** were synthesized as outlined in Scheme 1. Pentane-2,4-dione (**1**) underwent regioselective chlorination at the activated methylene position upon treatment with sulfuryl chloride in toluene at 0 °C for 12 h, affording 3-chloropentane-2,4-dione (**2**). Subsequent reaction of **2** with ammonia and carbon disulfide in ethanol at room temperature for 6 h generated the dithiocarbamate *in situ*, which cyclized to afford the 2-mercaptothiazole intermediate (**3**). Claisen–Schmidt condensation of **3** with the appropriate *para*-substituted benzaldehydes in ethanolic 60% NaOH at 0 °C for 18 h, then yielded the chalcone derivatives **4a–e** bearing the free mercapto group at the thiazole C2 position.

In parallel, the pyrazole fragment was prepared from the corresponding phenacyl bromides **5a–c**. Nucleophilic substitution of **5a–c** with potassium cyanide in ethanol at 50 °C for 2 h afforded the β-ketonitriles **6a–c**, which then underwent cyclocondensation with phenylhydrazine hydrochloride under reflux for 8 h to yield the amino pyrazoles **7a–c**. *N*-acylation of the

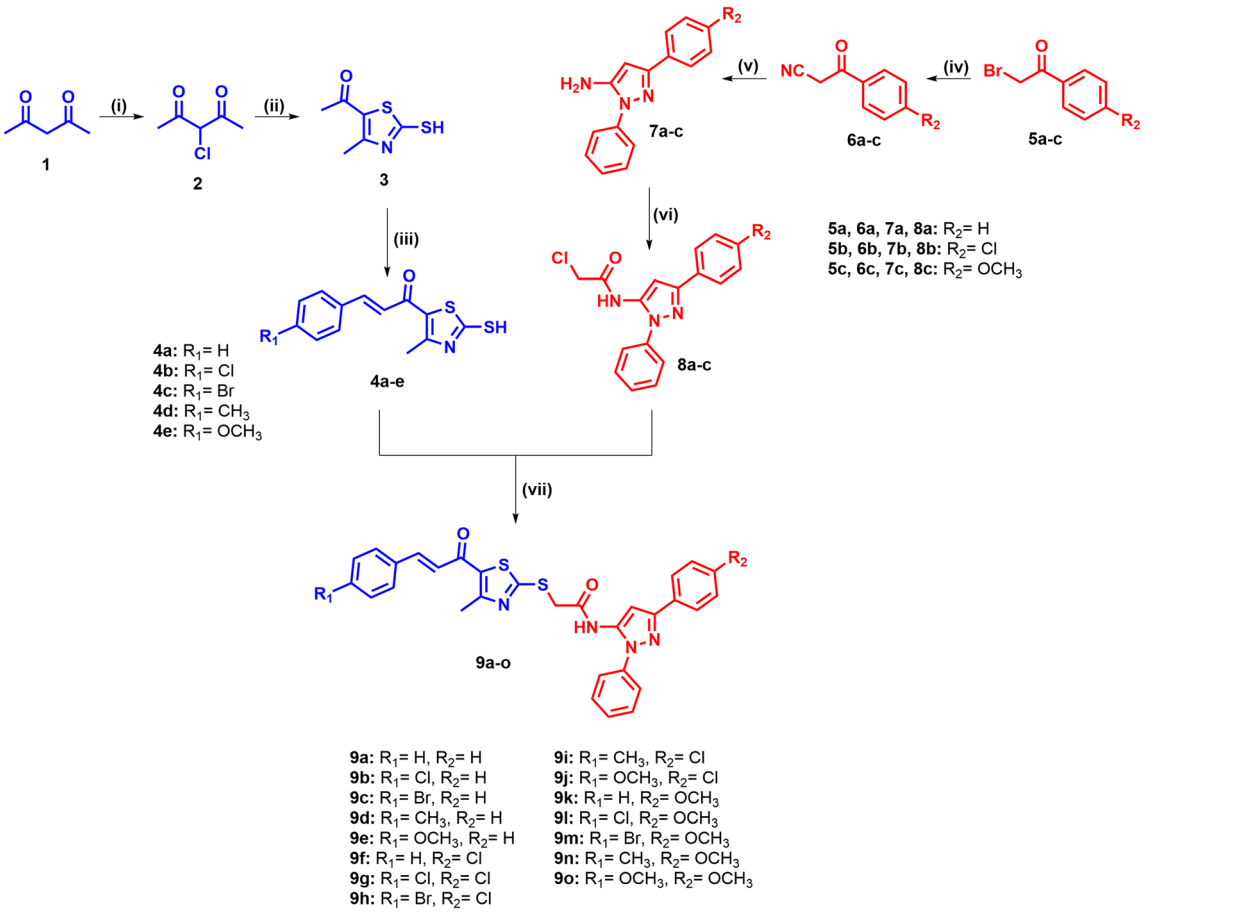

Scheme 1 Synthesis of the thiazole chalcone/pyrazole hybrids **9a–o**.

amino group in **7a–c** was achieved with chloroacetyl chloride in dichloromethane at 0 °C for 12 h, giving the key chloroacetamido pyrazoles **8a–c**. The final step involved *S*-alkylation of the mercaptochalcones **4a–e** with the α-chloroacetamides **8a–c** in acetonitrile containing triethylamine at room temperature for 6 h, affording the target compounds **9a–o**.

2.2 Reagents and conditions

(i) SO_2Cl_2, toluene, 0 °C, 12 h; (ii) NH_3, CS_2, EtOH, RT, 6 h; (iii) appropriate benzaldehyde derivative, 60% NaOH, EtOH, 0 °C, 18 h; (iv) KCN/ethanol, 50 °C, 2 h; (v) phenylhydrazine/HCl, reflux, 8 h; (vi) chloroacetyl chloride, DCM, 0 °C, 12 h; (vii) acetonitrile, TEA, RT, 6 h.

The synthesized compounds **9a–o** were characterized by ^{1}H NMR, ^{13}C NMR, and elemental analysis. The ^{1}H NMR spectra, recorded in DMSO-d_6, exhibited characteristic signals consistent with the proposed structures. A downfield broad singlet for the amide NH proton was observed at δ 10.45–10.56 ppm. The pyrazole C4-H resonated as a singlet between δ 6.82 and 6.94 ppm. The aromatic protons of the three phenyl rings appeared in the region δ 6.95–7.86 ppm. The *trans* chalcone olefinic protons were observed as two doublets at δ 7.62–7.68 ppm and δ 7.17–7.35 ppm, confirming the (*E*)-geometry of the enone system. The thioacetamide methylene protons appeared as a sharp singlet at δ 4.25–4.26 ppm, while the thiazole methyl group gave a singlet at δ 2.62–2.63 ppm. In derivatives containing a *p*-methyl substituent, an additional singlet was observed at δ 2.32 ppm. Methoxy groups on the aromatic rings (when present) appeared as singlets in the range of δ 3.75–3.79 ppm.

The ^{13}C NMR spectra further supported the assigned structures, revealing two distinct carbonyl resonances: the chalcone ketone carbonyl at δ 181.71–181.97 ppm and the amide carbonyl at δ 168.21–168.98 ppm. The pyrazole C4 carbon appeared characteristically upfield at δ 99.31–99.99 ppm. The remaining aromatic carbons of the three phenyl rings and thiazole, along with the two olefinic chalcone carbons, resonated in the region δ 114.63–166.45 ppm. The thioacetamide methylene carbon was observed at δ 37.60–37.69 ppm, while the thiazole methyl carbon appeared at δ 18.72–18.84 ppm. When present, the *p*-methyl carbon resonated at δ 21.64–21.65 ppm and the methoxy carbons at δ 55.61–55.96 ppm. These spectral data collectively confirmed the successful formation of the target thiazole–pyrazole hybrids.

2.3 Biological evaluation

2.3.1. Antiproliferative activity. The antiproliferative activity of the synthesized hybrids **9a–o** was evaluated against three human cancer cell lines: MDA-MB-231 (triple-negative breast), HCA-7 (colon), and A549 (lung) carcinoma cell lines, with doxorubicin and combretastatin A-4 included as reference compounds (Table 1).

The parent compound **9a**, featuring unsubstituted phenyl rings at both positions (R_1 = H, R_2 = H), displayed the lowest activity within the series, exhibiting IC50 values of 11.92 ± 0.62, 15.84 ± 0.82, and 12.34 ± 0.64 μM against MDA-MB-231, HCA-7, and A549 cell lines, respectively. All substituted analogs showed improved activity relative to **9a**, confirming that modifications at both aromatic positions enhance the anticancer activity. Among monosubstituted compounds (R_2 = H), the potency order against MDA-MB-231 cells followed Br (**9c**, 5.21 ± 0.27 μM) > OCH_3 (**9e**, 4.86 ± 0.25 μM) > Cl (**9b**, 6.38 ± 0.33 μM) > CH_3 (**9d**, 8.42 ± 0.43 μM) > H (**9a**, 11.92 ± 0.62 μM). Statistical analysis of mean IC50 values by R_1 substituent confirmed that bromo substitution yielded the lowest average IC50 (3.53 ± 0.18 μM against MDA-MB-231), followed by chloro (4.39 ± 0.23 μM) and methoxy (4.41 ± 0.24 μM), whereas unsubstituted (8.95 ± 0.48 μM) and methyl (6.92 ± 0.36 μM) derivatives exhibited reduced potency. Notably, compound **9e** (R_1 = OCH_3, R_2 = H) demonstrated activity against HCA-7 cells (3.28 ± 0.17 μM) that surpassed doxorubicin (3.54 ± 0.36 μM) against this cell line.

Table 1 Antiproliferative activity of compounds **9a–o** against MDA-MB-231, HCA-7, and A549 cancer cell lines after 48 h treatment, expressed as IC_{50} values (μM) ± SEM, with doxorubicin and combretastatin A-4 as reference compounds

	Antiproliferative activity IC_{50} ± SEM (μM)		
Compound	MDA-MB-231	HCA-7	A549
9a	11.92 ± 0.62	15.84 ± 0.82	12.34 ± 0.64
9b	6.38 ± 0.33	8.76 ± 0.45	6.92 ± 0.36
9c	5.21 ± 0.27	7.42 ± 0.38	5.36 ± 0.28
9d	8.42 ± 0.43	10.48 ± 0.53	7.24 ± 0.37
9e	4.86 ± 0.25	3.28 ± 0.17	6.94 ± 0.35
9f	8.08 ± 0.41	6.54 ± 0.33	10.62 ± 0.54
9g	3.88 ± 0.20	4.92 ± 0.25	5.64 ± 0.29
9h	3.41 ± 0.17	4.36 ± 0.22	2.84 ± 0.14
9i	6.91 ± 0.35	5.86 ± 0.30	8.42 ± 0.43
9j	4.11 ± 0.21	3.14 ± 0.16	5.92 ± 0.30
9k	6.84 ± 0.35	5.12 ± 0.26	8.76 ± 0.44
9l	2.92 ± 0.15	2.18 ± 0.11	4.86 ± 0.25
9m	1.96 ± 0.10	2.57 ± 0.13	4.18 ± 0.21
9n	5.42 ± 0.27	4.26 ± 0.21	6.48 ± 0.33
9o	4.26 ± 0.21	3.02 ± 0.15	5.48 ± 0.28
Doxorubicin	1.62 ± 0.18	3.54 ± 0.36	4.96 ± 0.22
Combretastatin A-4	2.08 ± 0.27	1.91 ± 0.22	2.64 ± 0.24

Methoxy substitution at R_2 yielded the most potent compounds across all three cell lines, with disubstituted analogs showing superior activity to those bearing R_2 = Cl or single substitutions. Notably, compounds with R_2 = OCH_3 exhibited the lowest mean IC50 against MDA-MB-231 (4.28 ± 0.23 μM), compared to R_2 = Cl (5.28 ± 0.28 μM) and monosubstituted analogs (7.36 ± 0.40 μM). Compound **9m** (R_1 = Br, R_2 = OCH_3) emerged as the most potent compound overall in the series, displaying IC50 values of 1.96 ± 0.10, 2.57 ± 0.13, and 4.18 ± 0.21 μM against MDA-MB-231, HCA-7, and A549 cells, respectively. The activity of **9m** against MDA-MB-231 cells represented an 83.6% improvement over the parent compound **9a** and showed potency comparable to doxorubicin (1.62 ± 0.18 μM) and combretastatin A-4 (2.08 ± 0.27 μM). Compound **9l** (R_1 = Cl, R_2 = OCH_3) ranked as the second most potent analog overall, demonstrating IC50 values of 2.92 ± 0.15, 2.18 ± 0.11, and 4.86 ± 0.25 μM against MDA-MB-231, HCA-7, and A549,

respectively, with activity against HCA-7 cells exceeding that of doxorubicin (3.54 ± 0.36 μM).

Compound **9h** (R_1 = Br, R_2 = Cl) showed exceptional activity against A549 lung carcinoma cells (2.84 ± 0.14 μM) that exceeded its activity against the other two cell lines, indicating cell line-specific responses within the disubstituted series containing R_2 = Cl. MDA-MB-231 triple-negative breast cancer cells generally demonstrated the highest sensitivity to the compound series, exhibiting the lowest mean IC50 values across most substitution patterns. HCA-7 colon cancer cells showed intermediate sensitivity, while A549 lung carcinoma cells displayed the most variable responses, with certain compounds (particularly **9h**) showing exceptional activity while others demonstrated reduced potency.

2.3.2. Cytotoxicity against normal MCF-10A breast epithelial cells. The cytotoxicity of the target compounds (**9a–o**) against normal MCF-10A breast epithelial cells was evaluated to assess selectivity toward cancer cells. Selectivity indices (SI) were calculated as the ratio of IC50 values for MCF-10A cells to those for each cancer cell line, with doxorubicin and combretastatin A-4 included as reference compounds (Table 2).

The target compounds exhibited substantially lower cytotoxicity against MCF-10A normal cells than against cancer cell lines, with IC50 values ranging from 12.76 ± 0.46 μM (**9m**) to 24.24 ± 1.06 μM (**9a**). Doxorubicin showed an IC50 of 2.80 ± 0.25 μM against MCF-10A cells, indicating considerable toxicity toward normal cells. The selectivity indices for compounds **9a–9o** against MDA-MB-231 cells ranged from 2.03 (**9a**) to 6.51 (**9m**), with most analogs exceeding an SI value of 3.0. Doxorubicin demonstrated an SI of 1.73 against MDA-MB-231, while combretastatin A-4 showed an SI of 2.31. Against HCA-7 cells, doxorubicin exhibited an SI below 1 (0.79), indicating greater toxicity toward normal cells than this cancer cell line. All target compounds maintained SI values above 1.53, with compounds **9l** (6.84) and **9e** (5.77) showing favorable selectivity.

Compounds **9m** and **9l**, which demonstrated the highest antiproliferative potency against cancer cells, also exhibited the most favorable selectivity profiles. Compound **9m** showed SI values of 6.51, 4.96, and 3.05 against MDA-MB-231, HCA-7, and A549 cells, respectively, while compound **9l** displayed SI values of 5.11, 6.84, and 3.07 against the same cell lines. These values exceed those of doxorubicin across all three cancer cell lines and surpass those of combretastatin A-4 in MDA-MB-231 and A549 cells. Compound **9h** (R_1 = Br, R_2 = Cl) also demonstrated strong selectivity, with an SI of 4.85 against A549 cells, consistent with its activity against this cell line observed in the antiproliferative assay.

The selectivity indices against A549 lung carcinoma cells were generally lower than those observed for MDA-MB-231 and HCA-7 cells across the compound series, with values ranging from 1.96 (**9a**) to 4.85 (**9h**) compared to combretastatin A-4 (1.82) and doxorubicin (0.56). Compounds **9m** and **9l** achieved SI values above 3.0 against A549 cells, indicating acceptable selectivity margins for this cell line.

2.3.3. *In vitro* tubulin polymerization inhibitory assay. The effects of the synthesized hybrids **9a–o** on tubulin polymerization, using combretastatin A-4 (CA-4) as the reference inhibitor, are illustrated in Fig. 4. Compounds **9a–o** exhibited clear inhibitory activity against tubulin polymerization, with IC_{50} values ranging from 3.97 to 12.18 μM, compared to CA-4 (IC_{50} = 3.84 ± 0.28 μM). Among the tested derivatives, compounds **9m**, **9l**, **9h**, and **9g** were the most active, with IC_{50} values of 3.97 ± 0.24, 4.21 ± 0.25, 4.43 ± 0.27, and 4.96 ± 0.31 μM, respectively. In particular, **9m** exhibited the highest tubulin polymerization-inhibitory activity in the series and was only 1.03-fold less potent than CA-4, whereas **9l** and **9h** were 1.10-fold and 1.15-fold less potent than the reference compound, respectively.

Table 2 Cytotoxicity of compounds **9a–o** against normal MCF-10A breast epithelial cells after 48 h treatment, expressed as IC_{50} values (μM) ± SEM, together with their selectivity indices relative to MDA-MB-231, HCA-7, and A549 cancer cell lines; doxorubicin and combretastatin A-4 were included as reference compounds

		Selectivity index (SI)		
Compound	MCF-10A IC_{50} ± SEM (μM)	MDA-MB-231	HCA-7	A549
9a	24.24 ± 1.06	2.03	1.53	1.96
9b	19.31 ± 0.80	3.03	2.20	2.79
9c	16.94 ± 0.67	3.25	2.28	3.16
9d	20.34 ± 0.85	2.42	1.94	2.81
9e	18.92 ± 0.78	3.89	5.77	2.73
9f	21.86 ± 0.93	2.71	3.34	2.06
9g	15.43 ± 0.60	3.98	3.14	2.74
9h	13.78 ± 0.51	4.04	3.16	4.85
9i	17.94 ± 0.73	2.60	3.06	2.13
9j	16.74 ± 0.66	4.07	5.33	2.83
9k	20.88 ± 0.88	3.05	4.08	2.38
9l	14.92 ± 0.57	5.11	6.84	3.07
9m	12.76 ± 0.46	6.51	4.96	3.05
9n	18.08 ± 0.73	3.34	4.24	2.79
9o	16.02 ± 0.63	3.76	5.30	2.92
Doxorubicin	2.80 ± 0.25	1.73	0.79	0.56
Combretastatin A-4	4.80 ± 0.40	2.31	2.51	1.82

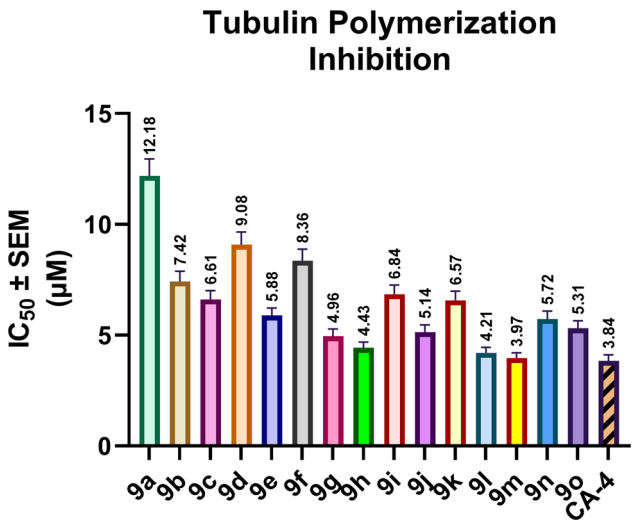

Fig. 4 Tubulin polymerization inhibitory activity of compounds **9a–o** and the reference inhibitor CA-4, expressed as IC_{50} values (μM), as determined from a fluorescence-based polymerization assay monitored kinetically for 60 min at 37 °C. Data are presented as mean ± SEM.

The anti-tubulin activity of compounds **9a–o** was markedly affected by the substitution pattern at both R_1 and R_2. When R_2 was kept unsubstituted, modification of the chalcone phenyl ring (R_1) produced a substantial enhancement in activity relative to the parent derivative **9a** ($IC_{50} = 12.18 \pm 0.76$ μM). Within this subset, compound **9e** ($R_1 = OCH_3$, $R_2 = H$) was the most active analogue, with an IC_{50} value of 5.88 ± 0.34 μM, followed by **9c** ($R_1 = Br$, $R_2 = H$; 6.61 ± 0.39 μM), **9b** ($R_1 = Cl$, $R_2 = H$; 7.42 ± 0.46 μM), and **9d** ($R_1 = CH_3$, $R_2 = H$; 9.08 ± 0.57 μM). Thus, when the pyrazole-linked phenyl ring remained unsubstituted, activity increased in the order $H < CH_3 < Cl < Br < OCH_3$.

A different but related trend was observed upon substitution at R_2 with chlorine. Compounds **9f–j**, bearing $R_2 = Cl$, showed improved activity relative to their corresponding $R_2 = H$ analogs. For example, the introduction of a chlorine substituent reduced the IC_{50} value from 12.18 to 8.36 μM for **9a**/**9f**, from 7.42 to 4.96 μM for **9b**/**9g**, from 6.61 to 4.43 μM for **9c**/**9h**, from 9.08 to 6.84 μM for **9d**/**9i**, and from 5.88 to 5.14 μM for **9e**/**9j**. Within this subgroup, activity followed the order $H < CH_3 < OCH_3 < Cl < Br$, with **9h** ($R_1 = Br$) and **9g** ($R_1 = Cl$) representing the most active derivatives.

The most favorable profile was obtained when R_2 carried a methoxy group. Compounds **9k–o**, bearing $R_2 = OCH_3$, constituted the most active subgroup overall, with IC_{50} values ranging from 3.97 to 6.57 μM. Within this subset, compound **9m** ($R_1 = Br$) was the most potent derivative in the entire series, followed by **9l** ($R_1 = Cl$), **9o** ($R_1 = OCH_3$), **9n** ($R_1 = CH_3$), and **9k** ($R_1 = H$). Direct comparison with the corresponding $R_2 = H$ analogs further demonstrated the favorable contribution of methoxy substitution at R_2. Thus, **9k** was 1.85-fold more potent than **9a**, **9l** was 1.76-fold more potent than **9b**, **9m** was 1.67-fold more potent than **9c**, **9n** was 1.59-fold more potent than **9d**, and **9o** was slightly more active than **9e**.

The tubulin polymerization results were also in good agreement with the antiproliferative data obtained against MDA-MB-231, HCA-7, and A549 cells. Compounds **9m** and **9l**, which displayed the highest tubulin polymerization inhibitory activity, were likewise the most potent antiproliferative derivatives in the cellular assay. In contrast, the weaker tubulin polymerization inhibitor **9a** displayed the lowest antiproliferative activity within the series. This parallel behavior supports the conclusion that inhibition of tubulin polymerization is a major contributor to the cytotoxic activity of these hybrids.

2.3.4. ***In vitro*** **COX inhibition assay.** The five most promising compounds, namely **9h**, **9j**, **9l**, **9m**, and **9o**, were selected for further evaluation of their inhibitory activity against COX-1 and COX-2, based on their superior antiproliferative activity and potent inhibition of tubulin polymerization. The obtained COX-1/COX-2 inhibitory profiles are illustrated in Fig. 5, while the corresponding selectivity indices are presented in Table 3. All the tested hybrids demonstrated preferential inhibition of COX-2 over COX-1, with COX-2 IC_{50} values spanning a submicromolar range (0.10–0.86 μM) and selectivity indices ranging from 9.79 to 109.20. In contrast, indomethacin exhibited a COX-2 SI of only 0.19, reflecting its well-established preferential inhibition of the constitutive COX-1 isoform.

Among the tested derivatives, compound **9l** ($R_1 = Cl$, $R_2 = OCH_3$) exhibited the most remarkable COX-2 inhibitory profile, with an IC_{50} value of 0.10 ± 0.01 μM that was comparable to that of the clinically approved selective COX-2 inhibitor celecoxib ($IC_{50} = 0.08 \pm 0.01$ μM), being only 1.25-fold less potent than the reference drug. Furthermore, **9l** displayed a COX-2 selectivity index of 109.20, which represents approximately 61% of celecoxib's SI (178.00) and is notably exceptional for a non-coxib scaffold devoid of the sulfonamide or methylsulfonyl pharmacophore that is classically considered essential for high COX-2 selectivity. This observation suggests that the chloro substituent on the chalcone phenyl ring, in conjunction with the methoxy group on the pyrazole-linked phenyl ring, provides

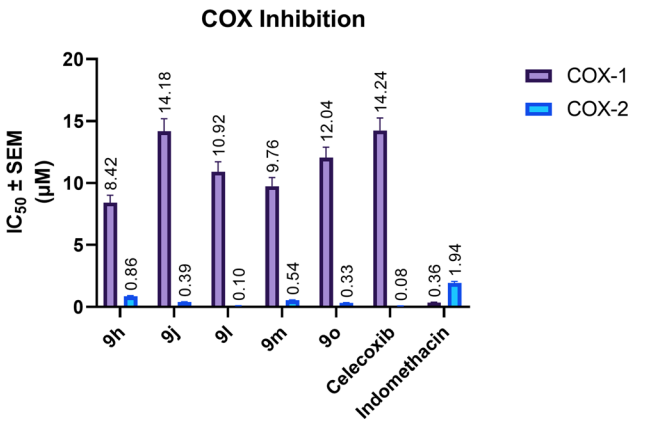

Fig. 5 COX-1 and COX-2 inhibitory activities of compounds **9h**, **9j**, **9l**, **9m**, and **9o**, compared with celecoxib and indomethacin, expressed as IC_{50} values (μM), obtained after 10 min compound/enzyme pre-incubation at 37 °C, 2 min arachidonic-acid reaction, and 15 min post-$SnCl_2$ incubation. Data are presented as mean ± SEM.

Table 3 COX-2 selectivity indices of selected compounds (**9h**, **9j**, **9l**, **9m**, and **9o**) compared with reference drugs (celecoxib and indomethacin), calculated from IC_{50} values obtained after 10 min compound/enzyme preincubation at 37 °C, 2 min arachidonic-acid reaction, and 15 min post-$SnCl_2$ incubation

Compound	COX-2 selectivity index
9h	9.79
9j	36.36
9l	109.20
9m	18.07
9o	36.48
Celecoxib	178.00
Indomethacin	0.19

a highly favorable substitution pattern for selective COX-2 inhibition. The relatively high COX-1 IC_{50} of **9l** (10.92 ± 0.78 μM) further contributes to its pronounced selectivity profile.

The remaining derivatives also demonstrated appreciable COX-2 inhibitory activity, with IC_{50} values of 0.33 ± 0.03, 0.39 ± 0.03, 0.54 ± 0.04, and 0.86 ± 0.06 μM for compounds **9o**, **9j**, **9m**, and **9h**, respectively. The overall COX-2 potency within the evaluated subset followed the order **9l** > **9o** > **9j** > **9m** > **9h**, while the corresponding selectivity indices decreased in the same order: 109.20, 36.48, 36.36, 18.07, and 9.79. All five compounds surpassed the COX-2 potency of indomethacin (IC_{50} = 1.94 ± 0.14 μM) by margins ranging from 2.3-fold (**9h**) to 19.4-fold (**9l**), and all exhibited substantially superior selectivity profiles relative to the non-selective reference.

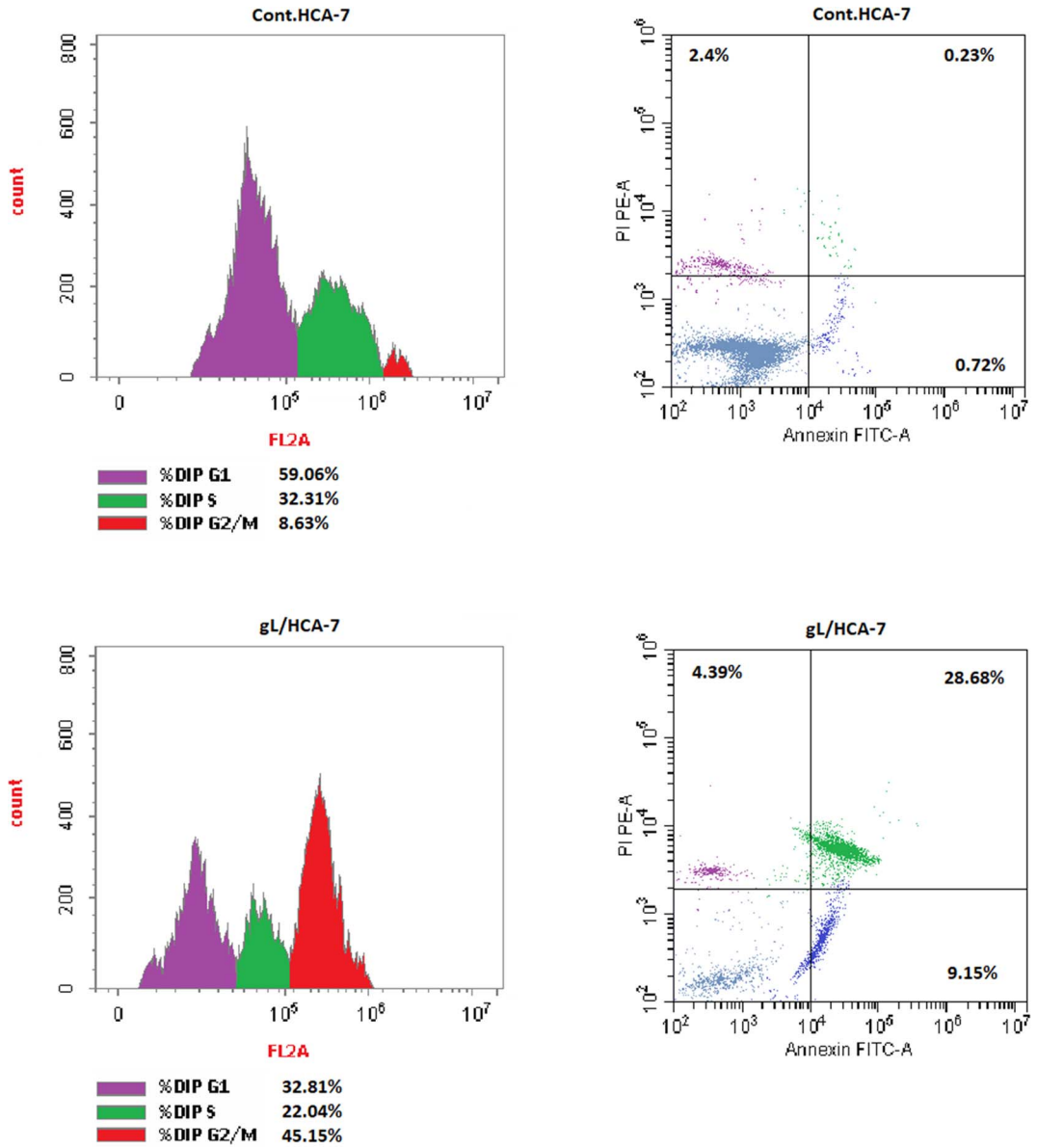

Fig. 6 Effect of compound **9l** on cell-cycle progression and apoptosis in HCA-7 cells after 48 h treatment at its IC_{50} concentration. Left panels show PI-based cell-cycle distribution, while right panels represent Annexin V-FITC/PI analysis of apoptotic populations.

2.3.5. Cell cycle analysis and apoptosis. Flow-cytometric analysis of PI-stained HCA-7 cells showed that treatment with **9l** markedly altered cell-cycle distribution. The cell-cycle data are illustrated in Fig. 6 and summarized in Table 4. Compared with the untreated control, **9l** reduced the G0/G1 population from 59.06% to 32.81% and the S-phase fraction from 32.31% to 22.04%, while markedly increasing the G2/M population from 8.63% to 45.15%. This pronounced accumulation of cells at the G2/M phase indicates that **9l** induced cell-cycle arrest at this stage. Such a profile is consistent with the anti-mitotic behavior expected for tubulin-targeting agents. It also supports the tubulin polymerization data, indicating that disruption of mitotic progression is a major contributor to the anti-proliferative effect of **9l** in HCA-7 cells.

Annexin V-FITC/PI double staining further demonstrated that the growth-inhibitory effect of **9l** was primarily mediated through induction of apoptotic cell death. The apoptotic distributions of treated and untreated cells are shown in Fig. 6 and summarized in Table 5. Treatment with **9l** increased the early and late apoptotic populations to 9.15% and 28.68%, respectively, whereas the necrotic population remained limited at 4.39%. In contrast, the untreated control showed only 0.72% early apoptosis, 0.23% late apoptosis, and 2.40% necrosis. The marked elevation in the apoptotic fractions, together with the predominance of late apoptosis over early apoptosis, indicates efficient progression of HCA-7 cells toward irreversible apoptosis rather than nonspecific cytotoxic injury.

Table 4 Effect of compound **9l** on cell-cycle distribution in HCA-7 cells after 48 h treatment at its IC_{50} concentration, expressed as percentages of cells in G0/G1, S, and G2/M phases

	DNA content		
Compound no.	% G0–G1	% S	% G2/M
Compound **9l**	32.81	22.04	45.15
DMSO (control)	59.06	32.31	8.63

Table 5 Effect of compound **9l** on apoptosis in HCA-7 cells after 48 h treatment at its IC_{50} concentration, expressed as percentages of total apoptotic, early apoptotic, late apoptotic, and necrotic cell populations

	Apoptosis			
Compound no.	Total	Early	Late	Necrosis
Compound **9l**	42.22	9.15	28.68	4.39
DMSO (control)	3.35	0.72	0.23	2.4

2.3.6. Effect of compound 9l on Bax and Bcl-2 protein expression. The effect of compound **9l** on the expression levels of the pro-apoptotic protein Bax and the anti-apoptotic protein Bcl-2 was assessed in HCA-7 cells (Table 6). Bax and Bcl-2 are key regulators of apoptosis, with Bax promoting and Bcl-2 inhibiting cell death. Accordingly, the Bax/Bcl-2 ratio represents a critical determinant of cellular fate, particularly in cancer cells where apoptotic pathways are frequently dysregulated.

The results indicated a significant increase in Bax protein levels following treatment with compound **9l**, with a concentration of 438.64 ± 15.72 pg mL^{-1}, representing a 5.63-fold increase compared to the DMSO control. This finding aligns with Bax's role as a pro-apoptotic factor that triggers the intrinsic apoptosis pathway by promoting mitochondrial cytochrome c release, ultimately leading to caspase activation and cell death. The upregulation of Bax suggests that compound **9l** may induce apoptosis *via* mitochondrial pathways, a desirable feature for anticancer agents aiming to selectively eliminate tumor cells.

Conversely, compound **9l** caused a marked reduction in Bcl-2 levels, with a concentration of 6.74 ± 0.19 pg mL^{-1}, indicating a 0.332-fold change relative to the control. Bcl-2 is known to prevent apoptosis by inhibiting the release of cytochrome c from mitochondria and blocking caspase activation. The observed downregulation of Bcl-2 by compound **9l** could further enhance the pro-apoptotic environment in treated cells, as decreased Bcl-2 levels would diminish its antagonistic effect on Bax, thereby facilitating apoptosis.

2.3.7. Effect of compound 9l on caspase-3 and caspase-9 levels. The impact of compound **9l** on apoptotic signaling was assessed through caspase-3 and caspase-9 assays, providing further evidence of its potential as a dual tubulin/COX-2 inhibitor with pronounced pro-apoptotic activity (Table 7). Caspase-9 acts as an initiator caspase, while caspase-3 functions as an executioner within the apoptotic cascade, and the marked elevation of both enzymes reflects activation of the intrinsic apoptotic pathway.

In HCA-7 cells, treatment with compound **9l** resulted in a substantial increase in caspase-3 levels to 496.80 ± 14.90 pg mL^{-1}, corresponding to an 8.54-fold rise relative to the DMSO control. This elevation confirms progression toward the execution phase of apoptosis and highlights the compound's ability to promote programmed cell death in cancer cells.

Consistently, caspase-9 levels increased to 47.86 ± 1.18 ng mL^{-1} (9.08-fold *vs.* control), indicating activation of the mitochondrial apoptotic pathway. This upregulation is associated with mitochondrial perturbation, leading to cytochrome c release, apoptosome formation, and subsequent activation of

Table 6 Effect of compound **9l** on Bax and Bcl-2 protein expression levels in HCA-7 cells after 48 h treatment at its IC_{50} concentration, relative to the DMSO-treated control

Compound	Bax (pg μL^{-1}) ± SEM	Fold change	Bcl-2 (pg μL^{-1}) ± SEM	Fold change
Compound **9l**	438.64 ± 15.72	5.63	6.74 ± 0.19	0.332
DMSO (control)	77.94 ± 2.08	1.00	20.32 ± 0.46	1.00

Table 7 Effect of compound **9l** on caspase-3 and caspase-9 levels in HCA-7 cells after 48 h treatment at its IC_{50} concentration, relative to the DMSO-treated control

Compound	Caspase-3 (pg mL^{-1}) ± SEM	Fold change	Caspase-9 (ng mL^{-1}) ± SEM	Fold change
Compound **9l**	496.80 ± 14.90	8.54	47.86 ± 1.18	9.08
DMSO (control)	58.16 ± 1.62	1.00	5.27 ± 0.23	1.00

Table 8 Effect of compound **9l** on extracellular PGE-2 production in HCA-7 cells after 24 h treatment with compound **9l** (1.0 μM), relative to the untreated control

Compound	PGE-2 level (ng mL^{-1})	Fold change	Relative PGE-2 production	Inhibition of PGE-2 release (%)
Untreated control	5.16 ± 0.18	1.00	100.0	0.0
Compound **9l**	0.56 ± 0.04	0.11	10.8	89.2

the caspase cascade. Collectively, these findings confirm that compound **9l** effectively induces apoptosis *via* the intrinsic mitochondrial pathway.

2.3.8. Effect of compound 9l on PGE-2 production. The effect of compound **9l** on prostaglandin E2 (PGE-2) production was evaluated by quantifying its extracellular levels in HCA-7 cell culture supernatants using a competitive ELISA assay. PGE-2 is a key downstream mediator of cyclooxygenase-2 activity and plays a central role in tumor progression through its involvement in proliferation, angiogenesis, and resistance to apoptosis. The corresponding results are presented in Table 8.

Treatment with compound **9l** at 1.0 μM resulted in a pronounced suppression of PGE-2 release relative to the untreated control. In HCA-7 cells, **9l** reduced extracellular PGE-2 levels to 0.56 ± 0.04 ng mL^{-1}, corresponding to a 0.11-fold change and an 89.2% decrease compared to the control (5.16 ± 0.18 ng mL^{-1}). This substantial reduction demonstrates the ability of **9l** to effectively attenuate prostaglandin biosynthesis in intact cancer cells. This pronounced suppression is consistent with the previously established selective COX-2 inhibitory profile of **9l** and indicates effective inhibition of COX-2-mediated signaling in a cellular context. Moreover, the marked reduction in PGE-2 complements the observed anti-proliferative and pro-apoptotic effects, further supporting the multitarget anticancer potential of compound **9l**.

2.3.9. Effect of compound 9l on cell migration. The migratory response of HCA-7 cells to **9l** was further examined using the CytoSelect™ wound-healing assay, in which removal of the insert generates a defined 0.9 mm wound field that enables direct monitoring of cell migration into the gap over time. This assay is particularly relevant because reduced wound closure reflects impaired collective cell migration, a process closely linked to tumor invasion and metastatic dissemination.

As shown in Fig. 7, the results further demonstrated that **9l** significantly impaired the migratory capacity of HCA-7 cells. Compared with the untreated control, which showed almost complete wound closure after 72 h (97.04 ± 3.15%), treatment with **9l** reduced wound closure to 58.52 ± 1.88% (Fig. 8). This reduction was also reflected in the migrated cell area, which

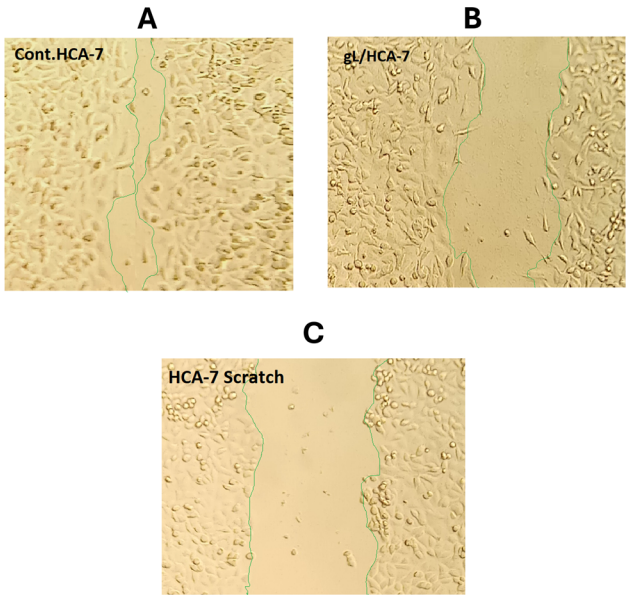

Fig. 7 Wound-healing images of HCA-7 cells after 72 h: (A) control, (B) **9l**-treated, and (C) initial wound field (0 h). Green lines indicate wound edges.

decreased from 0.786 in the control to 0.474 in the treated group, together with a clear reduction in migration length (ΔL = 0.4367 mm for control *vs.* 0.2633 mm for **9l**-treated cells). These findings indicate that **9l** markedly suppresses HCA-7 cell migration, further extending its anticancer profile beyond growth inhibition and apoptosis induction.

2.3.10. Metabolic stability of compound 9l in human liver microsomes. To assess its metabolic liability, the microsomal stability of compound **9l** was evaluated using pooled human liver microsomes under NADPH-supported oxidative conditions at substrate concentrations of 0.8, 4.0, and 20.0 μM. The obtained data are summarized in Table 9.

The results revealed a clear concentration-dependent improvement in apparent stability across the tested range. Increasing the starting concentration from 0.8 to 4.0 and 20.0

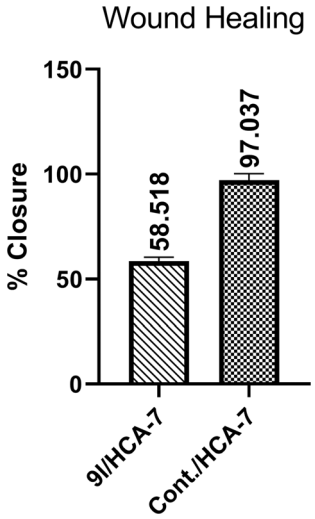

Fig. 8 Wound closure (%) of HCA-7 cells after 72 h treatment with **9l** *versus* control.

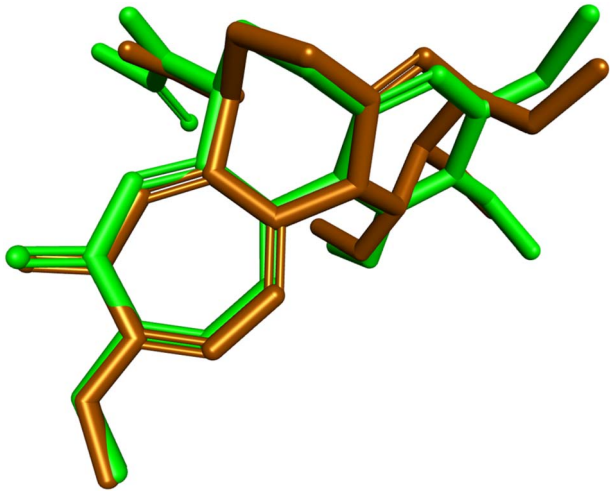

Fig. 9 Superimposition of the co-crystallized (green) and redocked (brown) colchicine poses within the colchicine-binding site of tubulin (PDB ID: 4O2B).

Table 9 Microsomal stability parameters of compound **9l** in pooled human liver microsomes at different starting concentrations, expressed as $t_{1/2}$ (h), intrinsic clearance (CLint; μL min^{-1} mg^{-1}), and percentage of parent compound remaining at 60 min

Start conc. (μM)	$t_{1/2}$ (h)	CLint (μL min^{-1} mg^{-1})	% Remaining at 60 min
0.8	0.542 ± 0.032	42.69 ± 2.55	28.0 ± 0.7
4.0	0.873 ± 0.013	26.46 ± 0.40	50.3 ± 1.2
20.0	1.321 ± 0.013	17.49 ± 0.18	61.0 ± 0.2

μM was associated with progressive prolongation of the half-life from 0.542 ± 0.032 h (32.5 ± 1.9 min) to 0.873 ± 0.013 h (52.4 ± 0.8 min) and 1.321 ± 0.013 h (79.3 ± 0.8 min), respectively. In parallel, the apparent intrinsic clearance decreased from 42.69 ± 2.55 to 26.46 ± 0.40 and 17.49 ± 0.18 μL min^{-1} mg^{-1}, while the percentage of parent compound remaining at 60 min increased from 28.0 ± 0.7% to 50.3 ± 1.2% and 61.0 ± 0.2%. This moderate-to-good profile, which improves at higher substrate levels consistent with possible enzyme saturation, falls within acceptable drug-like ranges and supports its suitability as a promising anticancer lead with acceptable metabolic stability under the tested *in vitro* conditions.

2.4 Computational studies

2.4.1. Molecular docking

2.4.1.1. Docking into the colchicine-binding site of tubulin. To clarify the molecular basis of the potent anti-tubulin activity of compound **9l**, docking studies were performed within the colchicine-binding site of tubulin (PDB ID: 4O2B).[44] The docking protocol was first validated by redocking the co-crystallized ligand colchicine into its native binding pocket. Superimposition of the redocked and crystallographic poses gave an RMSD value of 0.7508 Å, confirming the reliability of the adopted docking procedure. The predicted binding affinity of colchicine was −8.4 kcal mol^{-1}. The validation result is shown in Fig. 9.

Docking of compound **9l** into the same binding cavity afforded a predicted binding affinity of −9.6 kcal mol^{-1}, indicating a theoretically more favorable interaction than colchicine. Examination of the best-ranked pose revealed that **9l** was well accommodated within the colchicine pocket and formed multiple stabilizing interactions, predominantly hydrophobic in nature. The pyrazole ring established π–sigma interaction with Leu255, π–alkyl interaction with Leu242, and π–lone pair interaction with Val238. The two pyrazole-linked phenyl rings further reinforced binding through several hydrophobic contacts with Ala250, Cys241, Leu242, Leu255, Val238, Thr239, and Leu252, indicating efficient occupation of the hydrophobic region of the binding site.

Additional stabilization was provided by the methoxy substituent on the pyrazole-linked phenyl ring, which formed hydrophobic contacts with Leu242, Leu252, and Ile4, together with carbon–hydrogen bond interactions with Tyr52 and Gln136. Notably, the amidic NH formed a classical hydrogen bond with Val238, which may play an important role in anchoring the ligand within the pocket. The thiazole ring also contributed to binding through hydrophobic interactions with Ala316, Ala354, and Lys352, while the chalcone phenyl ring interacted with Lys352, Met259, and Val181. Moreover, the chloro substituent on the chalcone phenyl ring formed additional lipophilic contacts with Phe404, Ile347, and Val181. These results suggest that **9l** binds favorably within the colchicine site, consistent with its potent tubulin polymerization inhibitory and antiproliferative activities. The detailed binding interactions are shown in Fig. 10.

2.4.1.2. Docking into COX-2 enzyme. To investigate the second intended pharmacological target, compound **9l** was docked into the active site of COX-2 (PDB ID: 1CX2).[31] The docking protocol was validated by redocking the co-crystallized ligand SC-558 into its native binding site. Superimposition of the redocked and crystallographic poses gave an RMSD value of 0.8631 Å, confirming the validity of the protocol for this target.

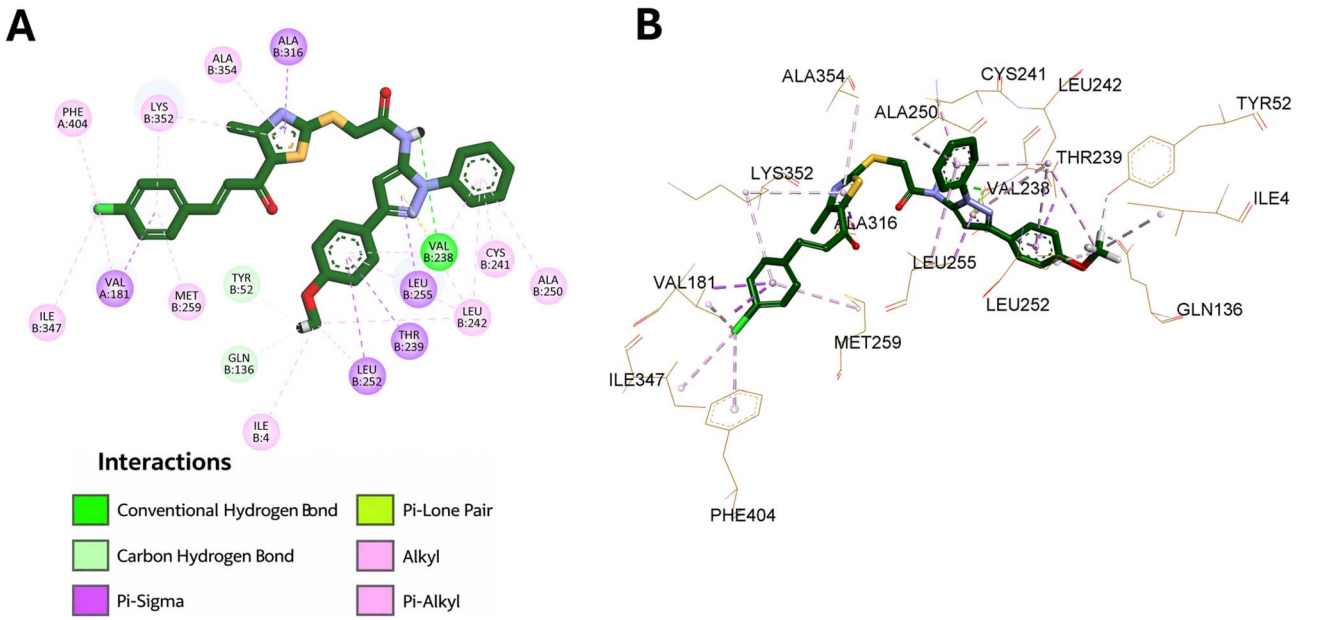

Fig. 10 Binding interactions of compound **9l** within the colchicine-binding site of tubulin (PDB ID: 4O2B): (A) 2D interaction diagram and (B) 3D binding mode.

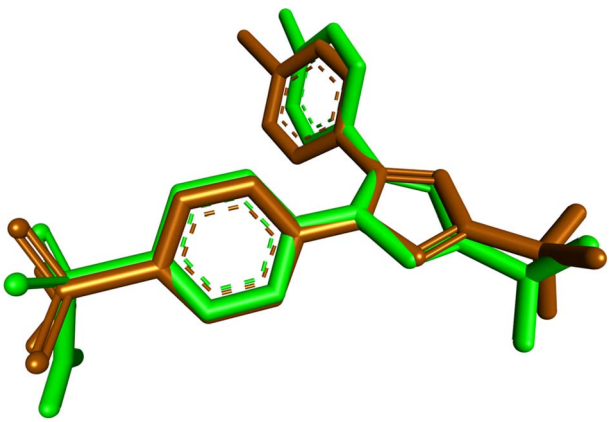

Fig. 11 Superimposition of the co-crystallized (green) and redocked (brown) SC-558 poses within the active site of COX-2 (PDB ID: 1CX2).

The predicted binding affinity of SC-558 was −10.3 kcal mol^{-1}. The superimposition result is presented in Fig. 11.

Compound **9l** exhibited a predicted binding affinity of −11.0 kcal mol^{-1}, suggesting a theoretically favorable interaction within the COX-2 active site. Analysis of the docked pose revealed that the pyrazole ring formed π–sigma interaction with Val349 and π–alkyl interaction with Ala527, while the two pyrazole-linked phenyl rings established multiple hydrophobic contacts with Val523, Ala527, Val349, Val116, Leu359, and Leu531. Additional stabilization arose from an amide–π stacked interaction with Gly526 and a π-donor non-classical hydrogen bond with Arg120.

The methoxy substituent on the pyrazole-linked phenyl ring further enhanced binding through hydrophobic interactions with Leu384, Tyr385, Phe381, and Trp387. In addition, the amidic carbonyl formed a classical hydrogen bond with Tyr355, which likely contributes to stabilization of the docked complex. The sulfur atom of the linker showed a sulfur–X interaction with Ser353, whereas the thiazole ring and its methyl substituent participated in several hydrophobic interactions with Ala516, Val523, Ile517, and Phe518. Moreover, the thiazole sulfur formed a π–sulfur interaction with His90. At the distal end, the chalcone phenyl ring interacted with Pro514, while its chloro substituent formed additional hydrophobic contacts with His95 and Pro514. These findings indicate that **9l** is well accommodated within the COX-2 active site, in agreement with its strong and selective COX-2 inhibitory activity. The interaction pattern of **9l** in the COX-2 active site is presented in Fig. 12.

2.4.1.3. In Silico ADMET prediction. The pharmacokinetic and safety-related properties of compound **9l** were preliminarily evaluated using the ADMETlab 3.0 platform.[45] The predicted profile revealed several favorable features supporting its potential as a bioactive lead. Compound **9l** showed a molecular weight of 599.11, TPSA of 74.08 Å^2, 6 hydrogen-bond acceptors, no hydrogen-bond donors, and 11 rotatable bonds, indicating acceptable polarity and flexibility. Although its lipophilicity was relatively high (log P = 6.03) and aqueous solubility was low (log S = −7.38), these features are consistent with the highly aromatic scaffold and may favor hydrophobic target binding.

This trend was also reflected in the ADMET radar plot (Fig. 13), where most properties were positioned within or close to the recommended physicochemical space, with the main deviations related to lipophilicity and distribution coefficient. Compound **9l** also showed no PAINS, BMS, or chelator alerts, together with very low probabilities of reactivity (0.02) and promiscuity (0.006), and remained synthetically accessible (Synth = 2).

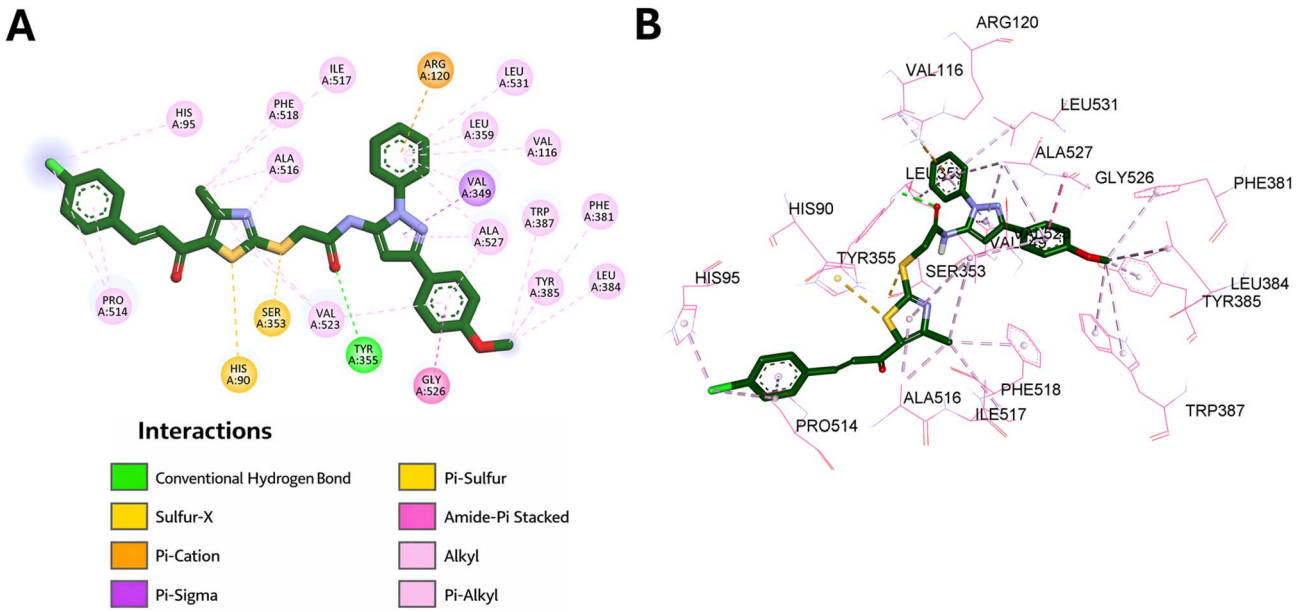

Fig. 12 Binding interactions of compound **9l** within the active site of COX-2 (PDB ID: 1CX2): (A) 2D interaction diagram and (B) 3D binding mode.

Absorption-related prediction was encouraging, with a low probability for poor intestinal absorption (HIA = 0.00), favorable oral bioavailability-related outputs (F20% = 0.00, F30% = 0.037, and F50% = 0.064), and non-substrate behavior toward *P*-glycoprotein (*P*-gp substrate = 0.00), although compound **9l** was predicted to act as a *P*-gp inhibitor (1.00). In addition, compound **9l** showed very low predicted BBB penetration (0.067), acceptable VDss (0.174 L kg^{-1}), a relatively high unbound fraction (Fu = 0.438), low probability of microsomal instability (0.256), and low predicted plasma clearance (2.571 mL min^{-1} kg^{-1}), despite a short predicted half-life (0.914 h).

On the toxicity side, several favorable predictions were obtained, including low probabilities for Ames mutagenicity (0.215), rat oral acute toxicity (0.163), eye corrosion (0.00), eye irritation (0.031), hematotoxicity (0.187), RPMI-8226 immunotoxicity (0.029), and A549 cytotoxicity (0.154). Although alerts were predicted for hERG liability and hepatotoxicity, these findings require experimental confirmation. Overall, the ADMETlab 3.0 results support compound **9l** as a synthetically feasible and pharmacologically promising lead.

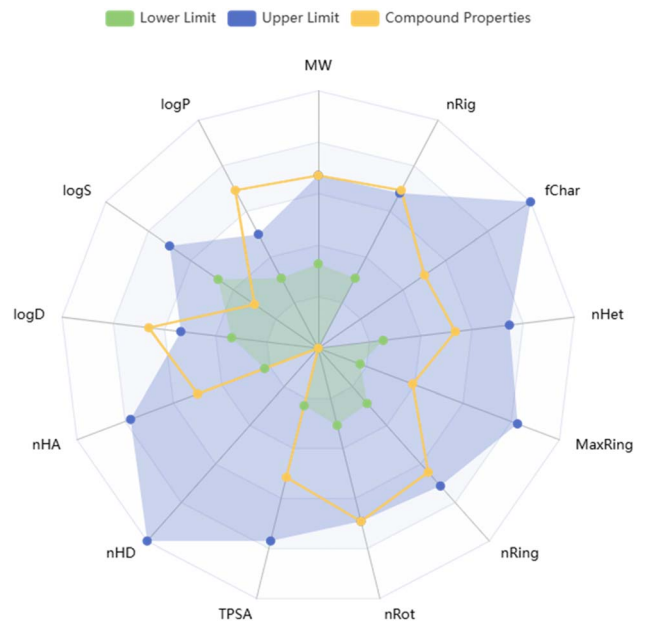

Fig. 13 ADMET radar plot of compound **9l** generated using ADMETlab 3.0, showing key physicochemical properties relative to the optimal drug-likeness space.

3. Conclusion

In conclusion, a new series of thiazole–chalcone/pyrazole hybrids (**9a–o**) was successfully designed, synthesized, and biologically evaluated as potential dual-acting anticancer agents targeting tubulin polymerization and COX-2. Several derivatives exhibited promising antiproliferative activity against MDA-MB-231, HCA-7, and A549 cancer cell lines, with improved selectivity over normal MCF-10A cells. Compounds **9m** and **9l** emerged as the most active members of the series. Among them, compound **9l** showed the most balanced biological profile, displaying potent tubulin polymerization inhibition, strong and selective COX-2 inhibition, marked suppression of PGE-2 production, induction of G2/M cell-cycle arrest, and pronounced apoptotic effects associated with Bax upregulation, Bcl-2 downregulation, and activation of caspase-3 and caspase-9. In addition, **9l** significantly inhibited HCA-7 cell migration, further supporting its anticancer potential. These experimental findings were consistent with the docking results, which demonstrated favorable accommodation of **9l** within both the colchicine-binding site of tubulin and the active site of COX-2. At the same time, ADMET prediction and human liver microsomal

stability studies suggested an acceptable drug-like and metabolic profile. Overall, compound **9l** represents a promising lead for further optimization as a multitarget anticancer agent.

4. Experimental

4.1 Chemistry

4.1.1 General details. Refer to SI.

3-Chloroacetylacetone (**2**),[46] 1-(2-mercapto-4-methylthiazol-5-yl)ethan-1-one (**3**) and chalcones (**4a–e**),[22] amino pyrazoles (**7a–c**) and chloroacetamides (**8a–c**)[40] were prepared according to reported methods.

4.1.2 General procedures for the synthesis of compounds 9a–o. To a well-stirred solution of the appropriate chalcones (**4a–e**) (1 mmol) and triethylamine (1.5 mmol, 0.152 mg) in acetonitrile, the pyrazole derivative (**8a–c**) (1 mmol) was added. The resulting clear mixture was stirred at room temperature for 6 hours. The formed precipitate was filtered off, washed with cold acetonitrile and distilled water, and dried. The crude product was recrystallized from acetonitrile/water.

4.1.3 2-((5-Cinnamoyl-4-methylthiazol-2-yl)thio)-*N*-(1,3-diphenyl-1*H*-pyrazol-5-yl)acetamide (9a). Yellow powder (396 mg, 74% yield), m.p. 219–221 °C; ^{1}H NMR (500 MHz, DMSO-d_6) δ (ppm): 10.51 (s, 1H), 7.85 (d, J = 8.5 Hz, 2H), 7.79–7.74 (m, 2H), 7.67 (d, J = 15.5 Hz, 1H), 7.56 (d, J = 7.6 Hz, 2H), 7.49–7.41 (m, 7H), 7.40–7.31 (m, 3H), 6.94 (s, 1H), 4.26 (s, 2H), 2.63 (s, 3H); ^{13}C NMR (120 MHz, DMSO-d_6) δ (ppm): 181.97, 168.77, 166.43, 158.48, 149.66, 144.23, 138.77, 137.48, 134.66, 133.14, 132.57, 132.10, 131.43, 129.75, 129.55, 129.31, 128.39, 128.32, 127.42, 124.86, 124.41, 99.91, 37.61, 18.79. Anal. Calcd. For $C_{32}H_{28}N_4O_4S_2$: C, 64.41; H, 4.73; N, 9.39. Found: C, 64.58; H, 4.59; N, 9.58. MS (ESI) calcd for $C_{32}H_{28}N_4O_4S_2$: 536.13, found $[M]^+$: 536.38.

4.1.4 (*E*)-2-((5-(3-(4-chlorophenyl)acryloyl)-4-methylthiazol-2-yl)thio)-*N*-(1,3-diphenyl-1*H*-pyrazol-5-yl)acetamide (9b). Yellow powder (445 mg, 78% yield), m.p. 227–230 °C; ^{1}H NMR (500 MHz, DMSO-d_6) δ (ppm): 10.56 (s, 1H), 7.85 (d, J = 7.1 Hz, 2H), 7.81 (d, J = 6.9 Hz, 2H), 7.65 (d, J = 15.7 Hz, 1H), 7.56 (d, J = 6.9 Hz, 2H), 7.52–7.42 (m, 6H), 7.40–7.31 (m, 3H), 6.93 (s, 1H), 4.26 (s, 2H), 2.62 (s, 3H); ^{13}C NMR (120 MHz, DMSO-d_6) δ (ppm): 181.85, 168.91, 166.45, 158.62, 149.65, 142.75, 138.77, 137.47, 135.92, 133.61, 133.13, 132.49, 132.09, 131.00, 129.74, 129.57, 129.29, 128.30, 127.42, 125.55, 124.38, 99.95, 37.61, 18.79. Anal. Calcd. for $C_{30}H_{23}ClN_4O_2S_2$: C, 63.09; H, 4.06; N, 9.81. Found: C, 62.95; H, 4.17; N, 9.63. MS (ESI) calcd for $C_{30}H_{23}ClN_4O_2S_2$: 570.10, found $[M]^+$: 571.07.

4.1.5 (*E*)-2-((5-(3-(4-bromophenyl)acryloyl)-4-methylthiazol-2-yl)thio)-*N*-(1,3-diphenyl-1*H*-pyrazol-5-yl)acetamide (9c). Yellow powder (473 mg, 77% yield), m.p. 226–228 °C; ^{1}H NMR (500 MHz, DMSO-d_6) δ (ppm): 10.54 (s, 1H, NH), 7.86 (d, J = 8.4 Hz, 2H), 7.74 (d, J = 7.9 Hz, 2H), 7.67–7.60 (m, 4H), 7.56 (d, J = 7.7 Hz, 2H), 7.49–7.43 (m, 4H), 7.40–7.34 (m, 2H), 6.94 (s, 1H), 4.26 (s, 2H), 2.63 (s, 3H); ^{13}C NMR (120 MHz, DMSO-d_6) δ (ppm): 181.90, 168.97, 166.40, 158.63, 149.62, 142.87, 138.77, 137.47, 133.98, 133.11, 132.52, 132.10, 131.25, 129.76, 129.30, 128.31, 127.43, 125.77, 125.62, 124.83, 124.40, 99.94, 37.60, 18.84. Anal. Calcd. for $C_{30}H_{23}BrN_4O_2S_2$: C, 58.54; H, 3.77; N, 9.10. Found: C, 58.72; H, 3.65; N, 9.01. MS (ESI) calcd for $C_{30}H_{23}BrN_4O_2S_2$: 614.04, found $[M]^+$: 614.30.

4.1.6 (*E*)-*N*-(1,3-diphenyl-1*H*-pyrazol-5-yl)-2-((4-methyl-5-(3-(*p*-tolyl)acryloyl)thiazol-2-yl)thio)acetamide (9d). Yellow powder (462 mg, 84% yield), m.p. 241–243 °C; ^{1}H NMR (500 MHz, DMSO-d_6) δ (ppm): 10.50 (s, 1H), 7.85 (d, J = 8.3 Hz, 2H), 7.66 (d, J = 7.5 Hz, 3H), 7.64–7.53 (m, 3H), 7.51–7.43 (m, 4H), 7.40–7.34 (m, 1H), 7.31–7.21 (m, 3H), 6.94 (s, 1H), 4.26 (s, 2H), 2.62 (s, 3H), 2.31 (s, 3H); ^{13}C NMR (120 MHz, DMSO-d_6) δ (ppm): 181.86, 168.52, 166.40, 158.30, 149.66, 144.32, 141.59, 138.81, 137.50, 133.13, 132.62, 132.12, 131.94, 130.16, 129.75, 129.35, 129.27, 128.29, 127.42, 124.42, 123.76, 99.85, 37.68, 21.65, 18.76. Anal. Calcd. for $C_{31}H_{26}N_4O_2S_2$: C, 67.61; H, 4.76; N, 10.17. Found: C, 67.45; H, 4.89; N, 10.37. MS (ESI) calcd for $C_{31}H_{26}N_4O_2S_2$: 550.15, found $[M]^+$: 550.69.

4.1.7 (*E*)-*N*-(1,3-diphenyl-1*H*-pyrazol-5-yl)-2-((5-(3-(4-methoxyphenyl)acryloyl)-4-methylthiazol-2-yl)thio)acetamide (9e). Yellow powder (475 mg, 84% yield), m.p. 236–238 °C; ^{1}H NMR (500 MHz, DMSO-d_6) δ (ppm): 10.50 (s, 1H), 7.85 (d, J = 5.9 Hz, 2H), 7.74 (d, J = 5.5 Hz, 2H), 7.64 (d, J = 16.0 Hz, 1H), 7.55 (d, J = 6.2 Hz, 2H), 7.49–7.34 (m, 6H), 7.19 (d, J = 14.4 Hz, 1H), 7.01–6.91 (m, 3H), 4.25 (s, 2H), 3.79 (s, 3H), 2.62 (s, 3H); ^{13}C NMR (120 MHz, DMSO-d_6) δ (ppm): 181.77, 168.21, 166.42, 162.14, 158.03, 149.66, 144.30, 138.82, 137.51, 133.14, 132.74, 132.12, 131.28, 129.74, 129.26, 128.28, 127.41, 127.27, 124.41, 122.26, 115.03, 99.82, 55.89, 37.67, 18.73. Anal. Calcd. for $C_{31}H_{26}N_4O_3S_2$: C, 65.70; H, 4.62; N, 9.89. Found: C, 65.81; H, 4.45; N, 10.03. MS (ESI) calcd for $C_{31}H_{26}N_4O_3S_2$: 566.14, found $[M]^+$: 566.56.

4.1.8 *N*-(3-(4-chlorophenyl)-1-phenyl-1*H*-pyrazol-5-yl)-2-((5-cinnamoyl-4-methylthiazol-2-yl)thio)acetamide (9f). Yellow powder (450 mg, 79% yield), m.p. 231–233 °C; ^{1}H NMR (500 MHz, DMSO-d_6) δ (ppm): 10.50 (s, 1H), 7.85 (d, J = 8.5 Hz, 2H), 7.80–7.75 (m, 2H), 7.67 (d, J = 15.6 Hz, 1H), 7.56 (d, J = 7.6 Hz, 2H), 7.48–7.41 (m, 6H), 7.39–7.31 (m, 3H), 6.94 (s, 1H), 4.26 (s, 2H), 2.63 (s, 3H); ^{13}C NMR (120 MHz, DMSO-d_6) δ (ppm): 181.82, 168.76, 166.38, 158.45, 149.66, 144.26, 138.81, 137.82, 134.69, 133.23, 133.12, 132.11, 131.47, 129.74, 129.55, 129.32, 128.30, 127.71, 127.44, 124.94, 124.43, 99.91, 37.64, 18.76. Anal. Calcd. for $C_{30}H_{23}ClN_4O_2S_2$: C, 63.09; H, 4.06; N, 9.81. Found: C, 62.88; H, 4.15; N, 9.68. MS (ESI) calcd for $C_{30}H_{23}ClN_4O_2S_2$: 572.10, found $[M+2H]^+$: 572.29.

4.1.9 (*E*)-*N*-(3-(4-chlorophenyl)-1-phenyl-1*H*-pyrazol-5-yl)-2-((5-(3-(4-chlorophenyl)acryloyl)-4-methylthiazol-2-yl)thio)acetamide (9g). Brown powder (466 mg, 77% yield), m.p. 205–207 °C; ^{1}H NMR (500 MHz, DMSO-d_6) δ (ppm): 10.56 (s, 1H), 7.85 (d, J = 8.4 Hz, 2H), 7.81 (d, J = 8.3 Hz, 2H), 7.65 (d, J = 15.5 Hz, 1H), 7.56 (d, J = 7.7 Hz, 2H), 7.50–7.43 (m, 6H), 7.38–7.33 (m, 2H), 6.93 (s, 1H), 4.26 (s, 2H), 2.63 (s, 3H); ^{13}C NMR (120 MHz, DMSO-d_6) δ (ppm): 181.88, 168.91, 166.47, 158.64, 149.62, 142.75, 138.78, 137.72, 137.51, 135.92, 131.08, 130.10, 129.74, 129.55, 129.27, 128.31, 128.27, 127.45, 125.60, 124.59, 124.39, 100.03, 37.67, 18.87. Anal. Calcd. for $C_{30}H_{22}Cl_2N_4O_2S_2$: C, 59.50; H, 3.66; N, 9.25. Found: C, 59.65; H, 3.56; N, 9.47. MS (ESI) calcd for $C_{30}H_{22}Cl_2N_4O_2S_2$: 604.06, found $[M]^+$: 604.44.

4.1.10 (*E*)-2-((5-(3-(4-bromophenyl)acryloyl)-4-methylthiazol-2-yl)thio)-*N*-(3-(4-chlorophenyl)-1-phenyl-1*H*-pyrazol-5-

yl)acetamide (9h). Brown powder (500 mg, 77% yield), m.p. 216–219 °C; ^{1}H NMR (500 MHz, DMSO-d_6) δ (ppm): 10.50 (s, 1H), 7.86 (d, J = 6.9 Hz, 2H), 7.74 (d, J = 6.9 Hz, 2H), 7.68–7.59 (m, 3H), 7.56 (d, J = 7.0 Hz, 2H), 7.50–7.43 (m, 4H), 7.36 (d, J = 11.8 Hz, 2H), 6.94 (s, 1H), 4.26 (s, 2H), 2.63 (s, 3H); ^{13}C NMR (120 MHz, DMSO-d_6) δ (ppm): 181.83, 168.92, 166.42, 158.65, 149.65, 142.84, 138.76, 137.47, 133.93, 133.13, 132.50, 132.07, 131.19, 129.75, 129.29, 128.31, 127.41, 125.57, 124.82, 124.39, 124.11, 99.87, 37.61, 18.77. Anal. Calcd. for $C_{30}H_{22}BrClN_4O_2S_2$: C, 55.43; H, 3.41; N, 8.62. Found: C, 55.31; H, 3.60; N, 8.51. MS (ESI) calcd for $C_{30}H_{22}BrClN_4O_2S_2$: 651.01, found $[M+3H]^+$: 651.58.

4.1.11 (*E*)-*N*-(3-(4-chlorophenyl)-1-phenyl-1*H*-pyrazol-5-yl)-2-((4-methyl-5-(3-(*p*-tolyl)acryloyl)thiazol-2-yl)thio)acetamide (9i). Brown powder (520 mg, 89% yield), m.p. 196–199 °C; ^{1}H NMR (500 MHz, DMSO-d_6) δ (ppm): 10.50 (s, 1H), 7.85 (d, J = 8.5 Hz, 2H), 7.65 (t, J = 11.9 Hz, 3H), 7.55 (d, J = 7.5 Hz, 2H), 7.48–7.42 (m, 4H), 7.39–7.34 (m, 1H), 7.28 (d, J = 15.5 Hz, 1H), 7.24 (d, J = 7.8 Hz, 2H), 6.94 (s, 1H), 4.26 (s, 2H), 2.63 (s, 3H), 2.32 (s, 3H); ^{13}C NMR (120 MHz, DMSO-d_6) δ (ppm): 181.95, 168.52, 166.41, 158.28, 149.65, 144.36, 141.62, 138.80, 137.49, 133.14, 132.64, 132.13, 131.97, 130.19, 129.76, 129.38, 129.30, 128.31, 127.44, 124.41, 123.86, 99.99, 37.69, 21.65, 18.78. Anal. Calcd. for $C_{31}H_{25}ClN_4O_2S_2$: C, 63.63; H, 4.31; N, 9.58. Found: C, 63.83; H, 4.18; N, 9.67. MS (ESI) calcd for $C_{31}H_{25}ClN_4O_2S_2$: 584.11, found $[M]^+$: 584.47.

4.1.12 (*E*)-*N*-(3-(4-chlorophenyl)-1-phenyl-1*H*-pyrazol-5-yl)-2-((5-(3-(4-methoxyphenyl)acryloyl)-4-methylthiazol-2-yl)thio) acetamide (9j). Yellow powder (444 mg, 74% yield), m.p. 216–219 °C; ^{1}H NMR (500 MHz, DMSO-d_6) δ (ppm): 10.50 (s, 1H), 7.85 (d, J = 8.5 Hz, 2H), 7.74 (d, J = 8.6 Hz, 2H), 7.64 (d, J = 15.4 Hz, 1H), 7.55 (d, J = 7.6 Hz, 2H), 7.50–7.41 (m, 4H), 7.39–7.34 (m, 1H), 7.19 (d, J = 15.4 Hz, 1H), 7.00–6.92 (m, 3H), 4.25 (s, 2H), 3.79 (s, 3H), 2.62 (s, 3H); ^{13}C NMR (120 MHz, DMSO-d_6) δ (ppm): 181.83, 168.26, 166.44, 162.15, 158.02, 149.64, 144.33, 138.79, 137.49, 133.12, 132.75, 132.11, 131.32, 129.76, 129.29, 128.30, 127.42, 127.27, 124.40, 122.30, 115.06, 99.92, 55.96, 37.63, 18.75. Anal. Calcd. for $C_{31}H_{25}ClN_4O_3S_2$: C, 61.94; H, 4.19; N, 9.32. Found: C, 61.75; H, 4.35; N, 9.10. MS (ESI) calcd for $C_{31}H_{25}ClN_4O_3S_2$: 601.11, found $[M + H]^+$: 601.50.

4.1.13 2-((5-Cinnamoyl-4-methylthiazol-2-yl)thio)-*N*-(3-(4-methoxyphenyl)-1-phenyl-1*H*-pyrazol-5-yl)acetamide (9k). Yellow powder (453 mg, 80% yield), m.p. 190–191 °C; ^{1}H NMR (500 MHz, DMSO-d_6) δ (ppm): 10.46 (s, 1H), 7.81–7.73 (m, 4H), 7.67 (d, J = 15.4 Hz, 1H), 7.55 (d, J = 8.0 Hz, 2H), 7.49–7.41 (m, 5H), 7.38–7.30 (m, 2H), 6.95 (d, J = 8.4 Hz, 2H), 6.82 (s, 1H), 4.26 (s, 2H), 3.75 (s, 3H), 2.64 (s, 3H); ^{13}C NMR (120 MHz, DMSO-d_6) δ (ppm): 181.90, 168.80, 166.38, 159.77, 158.51, 150.71, 144.21, 138.97, 137.13, 134.65, 132.55, 131.41, 129.70, 129.54, 129.30, 128.00, 127.06, 125.86, 124.81, 124.27, 114.63, 99.32, 55.61, 37.66, 18.78. Anal. Calcd. for $C_{31}H_{26}N_4O_3S_2$: C, 65.70; H, 4.62; N, 9.89. Found: C, 65.80; H, 4.41; N, 10.05. MS (ESI) calcd for $C_{31}H_{26}N_4O_3S_2$: 566.14, found $[M]^+$: 566.29.

4.1.14 (*E*)-2-((5-(3-(4-chlorophenyl)acryloyl)-4-methylthiazol-2-yl)thio)-*N*-(3-(4-methoxyphenyl)-1-phenyl-1*H*-pyrazol-5-yl)acetamide (9l). Yellow powder (456 mg, 76% yield), m.p. 214–216 °C; ^{1}H NMR (500 MHz, DMSO-d_6) δ (ppm): 10.51 (s, 1H), 7.81 (d, J = 7.9 Hz, 2H), 7.75 (d, J = 7.8 Hz, 2H), 7.65 (d, J = 15.5 Hz, 1H), 7.55 (d, J = 7.6 Hz, 2H), 7.50–7.42 (m, 4H), 7.39–7.30 (m, 2H), 6.95 (d, J = 7.8 Hz, 2H), 6.82 (s, 1H), 4.26 (s, 2H), 3.75 (s, 3H), 2.63 (s, 3H); ^{13}C NMR (120 MHz, DMSO-d_6) δ (ppm): 181.81, 168.92, 166.41, 159.78, 158.64, 150.69, 142.72, 138.97, 137.12, 135.92, 133.61, 132.45, 130.98, 129.69, 129.56, 127.99, 127.05, 125.87, 125.54, 124.24, 114.64, 99.45, 55.67, 37.67, 18.79. Anal. Calcd. for $C_{31}H_{25}ClN_4O_3S_2$: C, 61.94; H, 4.19; N, 9.32. Found: C, 61.81; H, 4.31; N, 9.15. MS (ESI) calcd for $C_{31}H_{25}ClN_4O_3S_2$: 600.11, found $[M]^+$: 600.81.

4.1.15 (*E*)-2-((5-(3-(4-bromophenyl)acryloyl)-4-methylthiazol-2-yl)thio)-*N*-(3-(4-methoxyphenyl)-1-phenyl-1*H*-pyrazol-5-yl)acetamide (9m). Yellow powder (477 mg, 74% yield), m.p. 206–208 °C; ^{1}H NMR (500 MHz, DMSO-d_6) δ (ppm): 10.46 (s, 1H), 7.77–7.71 (m, 4H), 7.66–7.60 (m, 3H), 7.55 (d, J = 7.6 Hz, 2H), 7.49–7.42 (m, 2H), 7.39–7.32 (m, 2H), 6.95 (d, J = 8.5 Hz, 2H), 6.82 (s, 1H), 4.26 (s, 2H), 3.76 (s, 3H), 2.63 (s, 3H); ^{13}C NMR (120 MHz, DMSO-d_6) δ (ppm): 181.71, 168.90, 166.36, 159.77, 158.68, 150.71, 143.11, 142.79, 138.96, 137.13, 133.89, 132.47, 131.12, 129.70, 128.00, 127.05, 125.86, 125.49, 124.82, 124.26, 114.63, 99.31, 55.61, 37.70, 18.79. Anal. Calcd. for $C_{31}H_{25}BrN_4O_3S_2$: C, 57.67; H, 3.90; N, 8.68. Found: C, 57.89; H, 3.81; N, 8.81. MS (ESI) calcd for $C_{31}H_{25}BrN_4O_3S_2$: 644.06, found $[M]^+$: 643.88.

4.1.16 (*E*)-*N*-(3-(4-methoxyphenyl)-1-phenyl-1*H*-pyrazol-5-yl)-2-((4-methyl-5-(3-(*p*-tolyl)acryloyl)thiazol-2-yl)thio)acetamide (9n). Brown powder (435 mg, 75% yield), m.p. 225–228 °C; ^{1}H NMR (500 MHz, DMSO-d_6) δ (ppm): 10.45 (s, 1H), 7.75 (d, J = 8.7 Hz, 2H), 7.65 (t, J = 11.9 Hz, 3H), 7.54 (d, J = 7.6 Hz, 2H), 7.45 (t, J = 7.7 Hz, 2H), 7.37–7.32 (m, 1H), 7.28 (d, J = 15.5 Hz, 1H), 7.24 (d, J = 7.8 Hz, 2H), 6.95 (d, J = 8.7 Hz, 2H), 6.82 (s, 1H), 4.25 (s, 2H), 3.76 (s, 3H), 2.63 (s, 3H), 2.32 (s, 3H); ^{13}C NMR (120 MHz, DMSO-d_6) δ (ppm): 181.92, 168.59, 166.41, 159.77, 158.34, 150.69, 144.36, 141.65, 138.94, 137.11, 132.61, 131.92, 130.19, 129.71, 129.37, 128.02, 127.06, 125.84, 124.25, 123.75, 114.64, 99.37, 55.62, 37.62, 21.64, 18.76. Anal. Calcd. for $C_{32}H_{28}N_4O_3S_2$: C, 66.19; H, 4.86; N, 9.65. Found: C, 66.08; H, 5.09; N, 9.50. MS (ESI) calcd for $C_{32}H_{28}N_4O_3S_2$: 580.16, found $[M]^+$: 580.44.

4.1.17 (*E*)-*N*-(3-(4-methoxyphenyl)-1-phenyl-1*H*-pyrazol-5-yl)-2-((5-(3-(4-methoxyphenyl)acryloyl)-4-methylthiazol-2-yl) thio)acetamide (9o). Yellow powder (477 mg, 80% yield), m.p. 220–221 °C; ^{1}H NMR (500 MHz, DMSO-d_6) δ (ppm): 10.46 (s, 1H), 7.78–7.71 (m, 4H), 7.64 (d, J = 15.4 Hz, 1H), 7.55 (d, J = 7.8 Hz, 2H), 7.49–7.41 (m, 2H), 7.38–7.31 (m, 1H), 7.19 (d, J = 15.4 Hz, 1H), 6.97 (dd, J = 11.6, 8.7 Hz, 4H), 6.82 (s, 1H), 4.25 (s, 2H), 3.78 (s, 3H), 3.75 (s, 3H), 2.62 (s, 3H); ^{13}C NMR (120 MHz, DMSO-d_6) δ (ppm): 181.81, 168.25, 166.40, 162.15, 159.79, 158.04, 150.70, 144.30, 138.98, 137.14, 132.74, 131.29, 129.70, 128.00, 127.27, 127.06, 125.89, 124.26, 122.30, 115.05, 114.64, 99.36, 55.95, 55.67, 37.66, 18.72. Anal. Calcd. for $C_{32}H_{28}N_4O_4S_2$: C, 64.41; H, 4.73; N, 9.39. Found: C, 64.58; H, 4.59; N, 9.58. MS (ESI) calcd for $C_{32}H_{28}N_4O_4S_2$: 596.16, found $[M]^+$: 596.99.

4.2 Biology

4.2.1. Antiproliferative activity. The antiproliferative activities of compounds **9a–o** were evaluated against MDA-MB-231, HCA-7, and A549 cancer cell lines, as well as MCF-10A normal

mammary epithelial cells, using the MTT assay (Sigma-Aldrich *In Vitro* Toxicology Assay Kit, MTT-based, TOX-1), with combretastatin A-4 and doxorubicin as reference drugs. IC_{50} values were determined from the corresponding dose–response curves. Further experimental details are provided in the SI.

4.2.2. Tubulin polymerization inhibitory assay. The effects of compounds **9a–o** on tubulin polymerization were assessed using a fluorescence-based tubulin polymerization assay (Cytoskeleton, Inc., Cat. No. BK011P), with combretastatin A-4 as the reference inhibitor. The inhibitory activities were expressed as IC_{50} values. Additional assay details are provided in the SI.

4.2.3. COX inhibition assay. The inhibitory activities of compounds **9h**, **9j**, **9l**, **9m**, and **9o** against COX-1 and COX-2 were evaluated using the Cayman COX (ovine/human) Inhibitor Screening Assay Kit (Item No. 560131). The inhibitory activities were expressed as IC_{50} values, and the selectivity index (SI) was calculated as IC_{50}(COX-1)/IC_{50}(COX-2). Further methodological details are given in the SI.

4.2.4. Cell cycle analysis and apoptosis. The effects of compound **9l** on cell-cycle progression and apoptosis in HCA-7 cells were analyzed by flow cytometry using propidium iodide staining and Annexin V-FITC/PI dual staining, respectively. The detailed experimental procedures are described in the SI.

4.2.5. Effect on Bax and Bcl-2 protein expression. The effect of compound **9l** on Bax and Bcl-2 protein expression in HCA-7 cells was evaluated using ELISA kits (DRG Human BAX ELISA Kit, Cat. No. EIA-4487; Zymed Bcl-2 ELISA Kit, Cat. no. 99-0042). Full assay details are provided in the SI.

4.2.6. Effect on Caspase-3 and Caspase-9 levels. The effects of compound **9l** on caspase-3 and caspase-9 levels in HCA-7 cells were determined using ELISA-based assays (Invitrogen Human Active Caspase-3 ELISA Kit, Cat. No. KHO1091; Thermo Fisher Human Caspase-9 ELISA Kit, Cat. No. BMS2025). Additional methodological details are given in the SI.

4.2.7. Effect on PGE-2 production. The effect of compound **9l** on PGE-2 production in HCA-7 cells was assessed using a competitive ELISA assay (R&D Systems Parameter™ PGE-2 Immunoassay, Cat. No. KGE004B). Further experimental details are provided in the SI.

4.2.8. Wound healing assay. The effect of compound **9l** on the migratory behavior of HCA-7 cells was evaluated using the CytoSelect™ 24-Well Wound Healing Assay (Cell Biolabs, Inc., Cat. No. CBA-120). The detailed experimental procedure is described in the SI.

4.2.9. Metabolic stability studies. The *in vitro* metabolic stability of compound **9l** was evaluated using pooled human liver microsomes under NADPH-supported oxidative conditions. Detailed incubation conditions, sample processing, and data analysis are provided in the SI.

4.3 Computational studies

The computational studies of compound **9l** comprised molecular docking and ADMET prediction. Docking against tubulin and COX-2 was performed using AutoDock Vina, with interaction analysis performed in Discovery Studio Visualizer, while ADMETlab 3.0 was used for *in silico* ADMET assessment. Full details are given in the SI.

Author contributions

conceptualization, B. A. A. S., K. S. A. and S. B.; methodology, B. A. A. S., A. A. Q., A. R. S., G. A. and A. A.; validation, K. S. A. and S. B.; formal analysis, A. A. Q., A. R. S., M. A.-Z., G. A. and A. A.; investigation, B. A. A. S., A. R. S., M. A.-Z., G. A. and A. A.; resources, A. A. Q., M. A.-Z. and S. B.; data curation, B. A. A. S. and M. A.-Z.; writing—original draft, B. A. A. S. and A. R. S.; writing—review and editing, K. S. A. and S. B.; supervision, K. S. A. and S. B.; project administration, A. A. Q.; funding acquisition, A. A. Q. All authors have read and agreed to the published version of the manuscript.

Conflicts of interest

The authors declare no conflicts of interest.

Data availability

The original contributions presented in this study are included in the article; further inquiries can be directed to the corresponding author.

Supplementary information (SI) is available. See DOI: https://doi.org/10.1039/d6ra03557d.

Acknowledgements

This work was supported and funded by the Deanship of Scientific Research at Imam Mohammad Ibn Saud Islamic University (IMSIU) (grant number IMSIU-DDRSP2601).

References

1 T. Mee, N. F. Kirkby, N. N. Defourny, K. J. Kirkby and N. G. Burnet, The Use of Radiotherapy, Surgery and Chemotherapy in the Curative Treatment of Cancer: Results from the FORTY (Favourable Outcomes from RadioTherapY) Project, *Br. J. Radiol.*, 2023, **96**, 20230334, DOI: 10.1259/bjr.20230334.

2 D. Hanahan, Hallmarks of Cancer: New Dimensions, *Cancer Discov.*, 2022, **12**, 31–46, DOI: 10.1158/2159-8290.CD-21-1059.

3 C. Holohan, S. Van Schaeybroeck, D. B. Longley and P. G. Johnston, Cancer Drug Resistance: An Evolving Paradigm, *Nat. Rev. Cancer*, 2013, **13**, 714–726, DOI: 10.1038/nrc3599.

4 H. Sung, J. Ferlay, R. L. Siegel, M. Laversanne, I. Soerjomataram, A. Jemal and F. Bray, Global Cancer Statistics 2020: GLOBOCAN Estimates of Incidence and Mortality Worldwide for 36 Cancers in 185 Countries, *CA Cancer J. Clin.*, 2021, **71**, 209–249, DOI: 10.3322/caac.21660.

5 A. Kabir and A. Muth, Polypharmacology: The Science of Multi-Targeting Molecules, *Pharmacol. Res.*, 2022, **176**, 106055, DOI: 10.1016/j.phrs.2021.106055.

6 A. Doostmohammadi, H. Jooya, K. Ghorbanian, S. Gohari and M. Dadashpour, Potentials and Future Perspectives of Multi-Target Drugs in Cancer Treatment: The next Generation Anti-Cancer Agents, *Cell Commun. Signal.*, 2024, **22**, 228, DOI: 10.1186/s12964-024-01607-9.

7 L. H. Al-Wahaibi, A. M. Elshamsy, T. F. S. Ali, B. G. M. Youssif, S. Bräse, M. Abdel-Aziz and N. A. El-Koussi, Design and Synthesis of New Dihydropyrimidine Derivatives with a Cytotoxic Effect as Dual EGFR/VEGFR-2 Inhibitors, *ACS Omega*, 2024, **9**, 34358–34369, DOI: 10.1021/acsomega.4c01361.

8 H. Hashem, A. M. Elshamsy, S. M. Rabea, A. A. Marzouk, S. Bräse, H. F. Hetta, A. Alkhammash, G. Alotaibi, H. M. Farhan and H. A. Aziz, Design, Synthesis, and Mechanistic Study of Novel Ciprofloxacin/Thiazole Chalcone Hybrids as Potential Anticancer Agents, *Pharmaceuticals*, 2025, **18**, 1700, DOI: 10.3390/ph18111700.

9 M. A. Jordan and L. Wilson, Microtubules as a Target for Anticancer Drugs, *Nat. Rev. Cancer*, 2004, **4**, 253–265, DOI: 10.1038/nrc1317.

10 A. Akhmanova and M. O. Steinmetz, Control of Microtubule Organization and Dynamics: Two Ends in the Limelight, *Nat. Rev. Mol. Cell Biol.*, 2015, **16**, 711–726, DOI: 10.1038/nrm4084.

11 M. Hawash, Recent Advances of Tubulin Inhibitors Targeting the Colchicine Binding Site for Cancer Therapy, *Biomolecules*, 2022, **12**, 1843, DOI: 10.3390/biom12121843.

12 J. Wang, D. D. Miller and W. Li, Molecular Interactions at the Colchicine Binding Site in Tubulin: An X-Ray Crystallography Perspective, *Drug Discov. Today*, 2022, **27**, 759–776, DOI: 10.1016/j.drudis.2021.12.001.

13 G. C. Tron, T. Pirali, G. Sorba, F. Pagliai, S. Busacca and A. A. Genazzani, Medicinal Chemistry of Combretastatin A4: Present and Future Directions, *J. Med. Chem.*, 2006, **49**, 3033–3044, DOI: 10.1021/jm0512903.

14 L. H. Al-Wahaibi, A. M. Elshamsy, T. F. S. Ali, B. G. M. Youssif, S. Bräse, M. Abdel-Aziz and N. A. El-Koussi, Design, Synthesis, and Antiproliferative Activity of Novel Thiazole-Based Derivatives as Tubulin Polymerization Inhibitors Targeting the Colchicine Binding Site, *RSC Adv.*, 2026, **16**, 25103–25115, DOI: 10.1039/D6RA01355D.

15 G. Wang, W. Liu, M. Fan, M. He, Y. Li and Z. Peng, Design, Synthesis and Biological Evaluation of Novel Thiazole-Naphthalene Derivatives as Potential Anticancer Agents and Tubulin Polymerisation Inhibitors, *J. Enzyme Inhib. Med. Chem.*, 2021, **36**, 1694–1702, DOI: 10.1080/14756366.2021.1958213.

16 M. Salehi, M. Amini, S. N. Ostad, G. H. Riazi, A. Assadieskandar, B. Shafiei and A. Shafiee, Synthesis, Cytotoxic Evaluation and Molecular Docking Study of 2-Alkylthio-4-(2,3,4-Trimethoxyphenyl)-5-Aryl-Thiazoles as Tubulin Polymerization Inhibitors, *Bioorg. Med. Chem.*, 2013, **21**, 7648–7654, DOI: 10.1016/j.bmc.2013.10.030.

17 S. Mahboobi, A. Sellmer, H. Höcher, E. Eichhorn, T. Bär, M. Schmidt, T. Maier, J. F. Stadlwieser and T. L. Beckers, [4-(Imidazole-1-Yl)Thiazol-2-Yl]Phenylamines. A Novel Class of Highly Potent Colchicine Site Binding Tubulin Inhibitors: Synthesis and Cytotoxic Activity on Selected Human Cancer Cell Lines, *J. Med. Chem.*, 2006, **49**, 5769–5776, DOI: 10.1021/jm060545p.

18 W. Liu, M. He, Y. Li, Z. Peng and G. Wang, A Review on Synthetic Chalcone Derivatives as Tubulin Polymerisation Inhibitors, *J. Enzyme Inhib. Med. Chem.*, 2022, **37**, 9–38, DOI: 10.1080/14756366.2021.1976772.

19 N. J. Lawrence, A. T. McGown, S. Ducki and J. A. Hadfield, The Interaction of Chalcones with Tubulin, *Anti-Cancer Drug Des.*, 2000, **15**, 135–141.

20 A. Kamal, M. Balakrishna, V. L. Nayak, T. B. Shaik, S. Faazil and V. D. Nimbarte, Design and Synthesis of Imidazo[2,1-b] Thiazole-Chalcone Conjugates: Microtubule-Destabilizing Agents, *ChemMedChem*, 2014, **9**, 2766–2780, DOI: 10.1002/cmdc.201402310.

21 F. Sultana, S. Reddy Bonam, V. G. Reddy, V. L. Nayak, R. Akunuri, S. Rani Routhu, A. Alarifi, M. S. K. Halmuthur and A. Kamal, Synthesis of Benzo[d]Imidazo[2,1-b] Thiazole-Chalcone Conjugates as Microtubule Targeting and Apoptosis Inducing Agents, *Bioorg. Chem.*, 2018, **76**, 1–12, DOI: 10.1016/j.bioorg.2017.10.019.

22 H. Hashem, A. Hassan, W. M. Abdelmagid, A. G. K. Habib, M. A. A. Abdel-Aal, A. M. Elshamsy, A. El Zawily, I. T. Radwan, S. Bräse, A. S. Abdel-Samea, *et al.*, Synthesis of New Thiazole-Privileged Chalcones as Tubulin Polymerization Inhibitors with Potential Anticancer Activities, *Pharmaceuticals*, 2024, **17**, 1154, DOI: 10.3390/ph17091154.

23 H. E. N. Khasawneh, E. I. Ali, R. M. Elmagzoub, R. F. A. Al-Aouadi, W. T. Almagharbeh, G. Alotaibi, S. Bräse and A. Alkhammash, A Novel Thiazole-Sulfonamide Hybrid Molecule as a Promising Dual Tubulin/Carbonic Anhydrase IX Inhibitor with Anticancer Activity, *Front. Chem.*, 2025, **13**, 1606848, DOI: 10.3389/fchem.2025.1606848.

24 B. A. A. Saleem, A. A. Qurtam, M. Ahmed, R. F. A. Al-Aouadi, A. A. A. Alrikabi, H. F. Hetta, S. Bräse, G. Alotaibi, A. Alkhammash and S. M. Farhan, Discovery of a Novel Coumarin/Thiazole Chalcone Hybrid as a Potent Dual Inhibitor of Tubulin and Carbonic Anhydrases IX & XII with Promising Anti-Proliferative Activity, *Molecules*, 2026, **31**, 917, DOI: 10.3390/molecules31060917.

25 L. H. Al-Wahaibi, A. M. Elshamsy, T. F. S. Ali, B. G. M. Youssif, S. Bräse, M. Abdel-Aziz and N. A. El-Koussi, Design, Synthesis, in Silico Studies, and Apoptotic Antiproliferative Activity of Novel Thiazole-2-Acetamide Derivatives as Tubulin Polymerization Inhibitors, *Front. Chem.*, 2025, **13**, 1565699, DOI: 10.3389/fchem.2025.1565699.

26 L. H. Al-Wahaibi, A. M. Elshamsy, T. F. S. Ali, B. G. M. Youssif, S. Bräse, M. Abdel-Aziz and N. A. El-Koussi, Development of a Novel Series of Thiazole-Based Compounds with Enhanced Antiproliferative Properties as Tubulin Polymerization Inhibitors, *Front. Chem.*, 2026, **14**, 1814119, DOI: 10.3389/fchem.2026.1814119.

27 A. Greenhough, H. J. M. Smartt, A. E. Moore, H. R. Roberts, A. C. Williams, C. Paraskeva and A. Kaidi, The COX-2/PGE2

Pathway: Key Roles in the Hallmarks of Cancer and Adaptation to the Tumour Microenvironment, *Carcinogenesis*, 2009, **30**, 377–386, DOI: 10.1093/carcin/bgp014.

28 L. S. Simon, Role and Regulation of Cyclooxygenase-2 during Inflammation, *Am. Med. J.*, 1999, **106**, 37S–42S, DOI: 10.1016/s0002-9343(99)00115-1.

29 B. Liu, L. Qu and S. Yan, Cyclooxygenase-2 Promotes Tumor Growth and Suppresses Tumor Immunity, *Am. Med. J.*, 2015, **15**, 106, DOI: 10.1186/s12935-015-0260-7.

30 N. U. A. Mohsin, S. Aslam, M. Ahmad, M. Irfan, S. A. Al-Hussain and M. E. A. Zaki, Cyclooxygenase-2 (COX-2) as a Target of Anticancer Agents: A Review of Novel Synthesized Scaffolds Having Anticancer and COX-2 Inhibitory Potentialities, *Pharmaceuticals*, 2022, **15**, 1471, DOI: 10.3390/ph15121471.

31 K. Rg, S. Am, G. Jk, M. Jj, S. Ra, P. Jy, G. D, M. Jm, P. Td, S. K, *et al.*, Structural Basis for Selective Inhibition of Cyclooxygenase-2 by Anti-Inflammatory Agents, *Nature*, 1996, **384**, 644–648, DOI: 10.1038/384644a0.

32 A. A. El-Malah, M. M. Gineinah, P. K. Deb, A. N. Khayyat, M. Bansal, K. N. Venugopala and A. S. Aljahdali, Selective COX-2 Inhibitors: Road from Success to Controversy and the Quest for Repurposing, *Pharmaceuticals*, 2022, **15**, 827, DOI: 10.3390/ph15070827.

33 K. Karrouchi, S. Radi, Y. Ramli, J. Taoufik, Y. N. Mabkhot, F. A. Al-Aizari and M. Ansar, Synthesis and Pharmacological Activities of Pyrazole Derivatives: A Review, *Molecules*, 2018, **23**, 134, DOI: 10.3390/molecules23010134.

34 R. Kumar, R. Sharma and D. K. Sharma, Pyrazole; A Privileged Scaffold of Medicinal Chemistry: A Comprehensive Review, *Curr. Top. Med. Chem.*, 2023, **23**, 2097–2115, DOI: 10.2174/1568026623666230714161726.

35 M. M. Ghoneim, M. A. Abdelgawad, N. A. A. Elkanzi and R. B. Bakr, Review of the Recent Advances of Pyrazole Derivatives as Selective COX-2 Inhibitors for Treating Inflammation, *Mol. Divers.*, 2025, **29**, 1789–1820, DOI: 10.1007/s11030-024-10906-9.

36 G. Li, Y. Cheng, C. Han, C. Song, N. Huang and Y. Du, Pyrazole-Containing Pharmaceuticals: Target, Pharmacological Activity, and Their SAR Studies, *RSC Med. Chem.*, 2022, **13**, 1300–1321, DOI: 10.1039/d2md00206j.

37 S. Bansal, M. Bala, S. K. Suthar, S. Choudhary, S. Bhattacharya, V. Bhardwaj, S. Singla and A. Joseph, Design and Synthesis of Novel 2-Phenyl-5-(1,3-Diphenyl-1H-Pyrazol-4-Yl)-1,3,4-Oxadiazoles as Selective COX-2 Inhibitors with Potent Anti-Inflammatory Activity, *Eur. J. Med. Chem.*, 2014, **80**, 167–174, DOI: 10.1016/j.ejmech.2014.04.045.

38 S.-Z. Ren, Z.-C. Wang, X.-H. Zhu, D. Zhu, Z. Li, F.-Q. Shen, Y.-T. Duan, H. Cao, J. Zhao and H.-L. Zhu, Design and Biological Evaluation of Novel Hybrids of 1, 5-Diarylpyrazole and Chrysin for Selective COX-2 Inhibition, *Bioorg. Med. Chem.*, 2018, **26**, 4264–4275, DOI: 10.1016/j.bmc.2018.07.022.

39 S. G. Alegaon, M. B. Hirpara, K. R. Alagawadi, K. K. Hullatti and K. Kashniyal, Synthesis of Novel Pyrazole–Thiadiazole Hybrid as Potential Potent and Selective Cyclooxygenase-2 (COX-2) Inhibitors, *Bioorg. Med. Chem. Lett.*, 2014, **24**, 5324–5329, DOI: 10.1016/j.bmcl.2014.08.062.

40 K. O. Farag, M. S. Nour, M. M. Abdelhafez, N. M. Ibrahim, H. A. Abdel-Aziz and S. H. Fahim, Pyrazole Derivatives as Dual COX-2/EGFR Inhibitors with Anticancer Potential: Optimization of Difenamizole Analogs, *Bioorg. Chem.*, 2026, **170**, 109444, DOI: 10.1016/j.bioorg.2025.109444.

41 M. S. Shaik, A. Chatterjee, T. Jackson and M. Singh, Enhancement of Antitumor Activity of Docetaxel by Celecoxib in Lung Tumors, *Int. J. Cancer*, 2006, **118**, 396–404, DOI: 10.1002/ijc.21325.

42 B. J. Schneider, G. P. Kalemkerian, M. J. Kraut, A. J. Wozniak, F. P. Worden, D. W. Smith, W. Chen and S. M. Gadgeel, PHASE II STUDY OF CELECOXIB AND DOCETAXEL IN NON-SMALL CELL LUNG CANCER (NSCLC) PATIENTS WITH PROGRESSION AFTER PLATINUM-BASED THERAPY, *J. Thorac. Oncol.*, 2008, **3**, 1454–1459, DOI: 10.1097/JTO.0b013e31818de1d2.

43 S. R. Olsen, Taxanes and COX-2 Inhibitors: From Molecular Pathways to Clinical Practice, *Biomed. Pharmacother.*, 2005, **59**(Suppl 2), S306–S310, DOI: 10.1016/s0753-3322(05)80052-6.

44 A. E. Prota, F. Danel, F. Bachmann, K. Bargsten, R. M. Buey, J. Pohlmann, S. Reinelt, H. Lane and M. O. Steinmetz, The Novel Microtubule-Destabilizing Drug BAL27862 Binds to the Colchicine Site of Tubulin with Distinct Effects on Microtubule Organization, *J. Mol. Biol.*, 2014, **426**, 1848–1860, DOI: 10.1016/j.jmb.2014.02.005.

45 L. Fu, S. Shi, J. Yi, N. Wang, Y. He, Z. Wu, J. Peng, Y. Deng, W. Wang, C. Wu, *et al.*, ADMETlab 3.0: An Updated Comprehensive Online ADMET Prediction Platform Enhanced with Broader Coverage, Improved Performance, API Functionality and Decision Support, *Nucleic Acids Res.*, 2024, **52**, W422–W431, DOI: 10.1093/nar/gkae236.

46 M. F. Abo-Ashour, W. M. Eldehna, R. F. George, M. M. Abdel-Aziz, M. M. Elaasser, N. M. Abdel Gawad, A. Gupta, S. Bhakta and S. M. Abou-Seri, Novel Indole-Thiazolidinone Conjugates: Design, Synthesis and Whole-Cell Phenotypic Evaluation as a Novel Class of Antimicrobial Agents, *Eur. J. Med. Chem.*, 2018, **160**, 49–60, DOI: 10.1016/j.ejmech.2018.10.008.